A proprioceptive feedback circuit controls *Caenorhabditis elegans* locomotor amplitude through dopamine signaling

Hongfei Ji[1], Anthony D. Fouad[1], Zihao Li[1], Andrew Ruba[1], and Christopher Fang-Yen[1,2,*]

[1]Department of Bioengineering, School of Engineering and Applied Science, University of Pennsylvania, Philadelphia, PA 19104.

[2]Department of Neuroscience, Perelman School of Medicine, University of Pennsylvania, Philadelphia, PA 19104.

*Correspondence: fangyen@seas.upenn.edu

ABSTRACT

Adaptive locomotion of animals depends on proprioception, which provides feedback on body postures to reshape motor output. How proprioception interacts with motor circuits and contributes to motor adaptation remains unclear. Here we characterize proprioception-mediated homeostatic control of undulatory movement in the roundworm *C. elegans*. The worm responds to optogenetically or mechanically induced decreases in mid-body bending amplitude by increasing its anterior amplitude. Conversely, it responds to increased mid-body amplitude by decreasing the anterior amplitude. This compensatory postural response requires dopaminergic PDE neurons to sense mid-body bending and signal to AVK interneurons via the D2-like dopamine receptor DOP-3. The FMRFamide-like neuropeptide FLP-1 from AVK regulates SMB head motor neurons to modulate anterior bending. We propose that this mechanism optimizes locomotion efficiency. Our findings demonstrate a functional motif for homeostatic behavioral control arising from the interplay between proprioception and neuromodulator signaling within a compact nervous system.

INTRODUCTION

Animal navigation in complex natural environments requires flexible and adaptable locomotor behavior[1]. During locomotion, an animal needs to adapt its body posture and motor output to its surrounding context and the inevitable perturbations resulting from obstacles and irregularities[2,3]. Kinematic and electromyographic studies in legged animals revealed phasic compensatory reactions in their central nervous systems, characterized by rapid corrective movements adapted to the perturbation[4,6,8,10]. In undulatory animals such as fish and nematodes, motor circuits also contextually tune motor behaviors to external conditions[5,7,9]. The observations of these adaptive movements in various conditions highlight the behavioral flexibility of motor systems across species.

In many animals, adaptive locomotory movements involve interactions between neural circuits called central pattern generators (CPGs) capable of generating primary locomotor rhythms[11–16] and sensory feedback that modulates locomotion[2,17–19]. In particular, proprioception provides rapid feedback on body position for locomotor control during natural movements[20–23]. In mammals, proprioceptive inputs from multiple sensory organs are continuously processed within spinal cord circuits to adapt motor behavior[24]. In lamprey and other undulators, locomotion also relies on proprioceptive feedback to adjust the undulatory gait to a changing physical environment[25–29].

The neural mechanisms underlying adaptive locomotion are complex and poorly understood. In vertebrates, the corrective locomotor control for handling perturbations during movements involves computations within circuits of the spinal cord, brain stem, and forebrain[13,30–32]. Recent genetic techniques have greatly facilitated the analyses of the function of CPGs in fine locomotor control and the identification of relevant neural components[17,33,34]. In the mouse, many spinal cord interneurons are essential for corrective locomotor control[35–40]. However, it is unclear how the identified neurons function in locomotor movements, partly because of the lack of *in vivo* methods for acutely interfering

with the neuronal activity[2]. Moreover, our knowledge of how proprioceptive input is relayed to control movement and posture and which circuit components are responsible for proprioceptive signal transmission remains minimal[41].

Here, we use the roundworm *C. elegans* to determine how corrective locomotor control is executed by nervous system. *C. elegans* has a relatively small and well-characterized connectome with fully identified cell types[42,43]. A wealth of methods for assaying and manipulating *C. elegans*[44–47] offers the unique opportunity for an integrative dissection of locomotor control at the systems, circuit, cellular, and molecular genetic levels.

C. elegans moves forward by propagating dorso-ventral flexions from anterior to posterior[48]. These undulatory movements are generated by sets of body wall muscles arranged in two dorsal and two ventral rows running along the length of the worm's body[49]. The alternating activity of antagonistic muscles is driven by motor neurons located in the head ganglia and the ventral nerve cord[50]. Proprioceptive coupling between ventral cord motor neurons is required for propagating undulatory waves along the body[51]. Motion direction is controlled by a set of premotor interneurons that coordinate forward and reverse locomotion[52].

While motor neurons and premotor interneurons are primarily responsible for generating worm's sinusoidal flexions[43,53], adaptive locomotion in natural contexts requires motor control of the head and involves sublateral motor neurons with various functional roles in modulating posture[54–57]. Context-dependent, optimal motor control is subject to feedback input from a large number of interneurons and sensory neurons[58–64], as well as neuromodulation by biogenic amines and neuropeptides that drive various long-term and short-term locomotor states[65–72].

In this work we used physical and optical perturbations to understand how the *C. elegans* motor system controls its bending amplitude during locomotion. Using targeted optogenetic manipulation in freely moving animals, we quantitatively analyze the consequent

locomotor dynamics and show that *C. elegans* uses a posterior-to-anterior proprioceptive feedback loop to adapt its locomotor amplitude to perturbations. We dissect the underlying neuronal pathway and find that dopaminergic PDE neurons are proprioceptors that sense mid-body curvature and drive AVK interneurons activity via the D2-like dopamine receptor DOP-3. AVK releases the FLP-1 FMRFamide-like neuropeptide, regulating downstream SMB head motor neurons to modulate anterior bending. Our findings identify a circuit for adaptive control of movement by *C. elegans* from sensory input to motor output. We discuss how this feedback control mechanism might help optimize locomotor efficiency and foraging behavior.

RESULTS

C. elegans bidirectionally modulates anterior bending amplitude in response to optogenetic perturbation of mid-body curvature.

To measure locomotor behavior, we calculate curvature along the worm body centerline[5] (Figure 1A). With this metric we quantified undulatory movements of freely moving *C. elegans* via the time-varying normalized curvature from head to tail (Figures 1C and F).

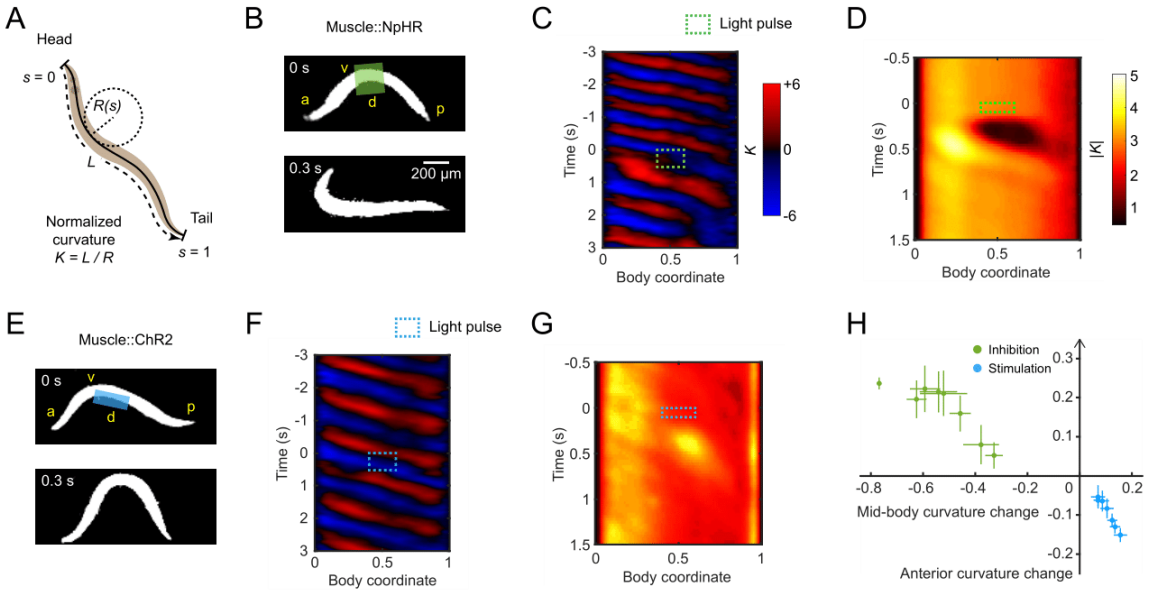

Figure 1. *C. elegans* bidirectionally modulates anterior bending amplitude in response to optogenetic perturbation of mid-body curvature.

(A) Quantification of worm locomotion using time-varying curvature. Body coordinate s is denoted by the distance along the centerline normalized by the body length L (head = 0, tail = 1). Normalized curvature K is the product of the body length and the reciprocal local radius of body curvature $R(s)$, with positive and negative values representing ventral and dorsal bending, respectively.

(B) Optogenetic muscle inhibition in the mid-body during forward locomotion. Green region indicates the laser illumination. a: anterior, p: posterior, d: dorsal, v: ventral.

(C) Curvature of the worm locomotion shown in (B). Green box indicates a 0.5 s laser illumination starting at $t = 0$ applied to the mid-body.

(D) Mean absolute curvature around 0.1 s inhibitions (green box). n = 1160 mid-body illuminations from 206 worms.

(E) Optogenetic muscle stimulation in the dorsal mid-body during forward locomotion. Blue region indicates the laser illumination.

(F) Curvature of the worm locomotion shown in (E). Blue box indicates a 0.5 s laser illumination starting at $t = 0$ applied to the dorsal mid-body.

(G) Mean absolute curvature around 0.1 s stimulations (blue box). n = 693 dorsal mid-body illuminations from 122 worms.

(H) Relationship between the mean normalized curvature change in the anterior vs. mid-body regions. Each point represents mean ± SEM of the corresponding normalized value of the first post-illumination curvature peak. Green and blue points denote data induced by optogenetic mid-body muscle inhibition (both sides) and stimulation (dorsal or ventral side), respectively. n = 110-150 illuminations from 10-20 animals per group.

In previous studies[27] we perturbed the muscular or neural activity in different body regions and analyzed the corresponding undulatory dynamics during forward locomotion. Using a laser targeting system[47,73] we applied green laser illumination (532 nm wavelength) to selected body regions of animals expressing the inhibitory opsin *NpHR* in body wall muscles (via the transgene *Pmyo-3::NpHR*).

Transient optogenetic inhibitions (0.1 or 0.5 s duration) of muscles at the head region (0.05-0.25 body length) or neck region (0.2-0.4 body length) both caused rapid straightening of the anterior region followed by a mild amplitude decline in the subsequent body bends propagating from head to tail (Figure S1A,B,E,F; Video S1), consistent with previous findings[27].

When inhibiting muscles at the mid-body (0.4-0.6 body length), in addition to a paralytic effect propagating from mid-body to tail, we observed exaggerated undulations at the anterior region (0.1-0.3 body length; Figures 1C,D, and S1G; Video S1). Worms returned to their baseline undulatory amplitude within about one undulatory cycle after the inhibition (Figures S1I,J).

We hypothesized that the increase in head bending represents a homeostatic response to decreased mid-body curvature. To test this idea, we asked how the animal would respond to an optogenetically induced increase in mid-body amplitude. We stimulated mid-body muscles on the dorsal or ventral side by illuminating the corresponding region of animals expressing the excitatory opsin *ChR2* in body wall muscles (via the transgene *Pmyo-3::ChR2*) using blue laser illumination (473 nm wavelength). While stimulating one side of muscles in the mid-body led to exaggerated mid-body bending, the anterior bending

amplitude decreased (Figures 1E-G, S1K,L; Video S2). These data show that anterior amplitude changes in the opposite direction as mid-body amplitude changes.

We also tested worm locomotion perturbed by brief muscle inhibition (0.1 s duration) at the posterior region (0.6-0.8 body coordinate). Posterior bending amplitude rapidly decreased upon illumination, but the bending amplitude of the anterior half did not increase (Figure S1D,H; Video S1). This result suggests that the anterior body bending responds to perturbations in the mid-body but not the posterior region.

We compared the sensitivity of the anterior response to stimulation versus inhibition in the mid-body muscles. We applied laser pulses to the mid-body with varied pulse duration and irradiance to change the degree of muscle stimulation or inhibition (see *Methods*). With the varying light dosage, changes in the anterior amplitude varied continuously in response to the induced changes in the mid-body amplitude (Figure 1H).

These observations indicate a mechanism that mediates anterior bending curvature in response to changes in mid-body curvature. Because the anterior curvature can be thought of as compensating for a change in mid-body curvature, we will henceforth refer to this effect as compensatory curvature response (CCR).

Physical constraint of mid-body causes an increase in anterior bending amplitude. We hypothesized that CCR requires proprioceptive sensing of mid-body curvature. In our optogenetic experiments, curvature change was induced by muscle activity manipulation, leaving the possibility that CCR arises from non-proprioceptive signaling within muscles or from muscles to neurons.

To test the involvement of proprioception in CCR, we designed a straight-channel microfluidic device that mechanically reduces mid-body bending amplitude by partially constraining this region (Figures 2A and S2A). In this manner, we manipulated body curvature without directly perturbing muscle activity.

During physical constraint, animals exhibited reduced bending amplitude in the constrained middle region and increased amplitude in the anterior region (Figures 2C and S2B; Video S3), similar to that observed during optogenetic muscle inhibition of the mid-body. These results show that CCR depends on proprioception.

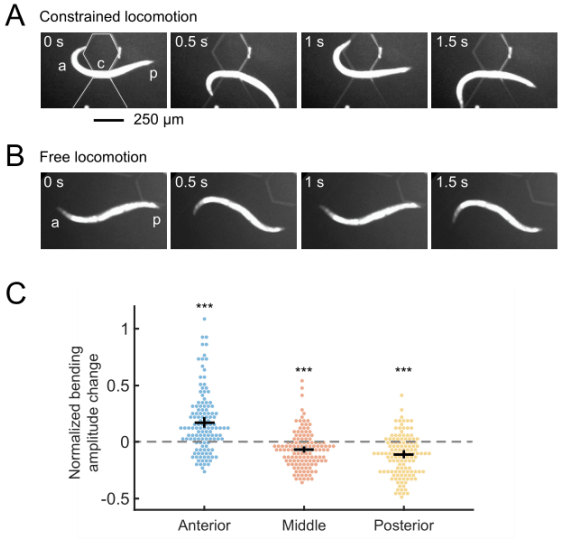

Figure 2. Physical constraint of mid-body causes an increase in anterior bending amplitude.

(A) A wild-type animal showing constrained locomotion with its mid-body confined by a straight-channel microfluidic device. a: anterior region, p: posterior region, c: constrained middle region of a worm.

(B) A wild-type animal during free locomotion in the wide region of the channel.

(C) Effects of mid-body constraint during forward locomotion on the undulatory bending amplitude of the anterior, middle, and posterior regions, measured as the normalized curvature change of the corresponding regions. n = 19 wild-type animals, mean ± SEM. ***p<0.001 compared with zero curvature change (gray line).

A candidate screen for genes required for compensatory curvature response

To understand the mechanisms underlying CCR, we screened candidate genes using the straight-channel microfluidic device. For each gene, we analyzed the anterior bending amplitude of the corresponding mutants constrained by the straight channel in the mid-body and compared it with the amplitude during free locomotion. We calculated a CCR index

equal to the difference between anterior bending amplitudes during constrained and free locomotion divided by the amplitude during free locomotion (see *Methods*).

In *C. elegans*, adjacent body wall muscle cells are connected by electrical synapses comprising the innexin UNC-9[74]. We tested whether these connections play any role in CCR. *unc-9* is expressed in body wall muscles and the nervous system. We used the microfluidic device to assay transgenic animals that were defective for UNC-9 in muscle cells but had functional UNC-9 in the nervous system[74] and found that they showed normal CCR (Figure S3B). This result indicates that CCR does not require direct inter-muscular coupling.

Several ion channels are involved in mechanosensation and proprioception, including members of degenerin/epithelial sodium (DEG/ENaC) channel and transient receptor potential (TRP) channel families[75]. We asked whether these channels are also required for CCR. We tested several DEG/ENaC and TRP channel mutants and found that all tested channel mutants showed CCR similar to wild-type animals (Figure S3A). A broader candidate screen of the mechanoreceptor mutants may be required to understand the mechanotransduction complexes associated with CCR.

Compensatory curvature response requires functional dopamine signaling by PDE neurons.

We asked what neurotransmitter systems might be required for CCR. We examined mutant strains with defects in the synthesis of biogenic amines, including dopamine (DA), serotonin (5-HT), tyramine (TA), octopamine (OA), and gamma-aminobutyric acid (GABA).

Mutants for *tph-1(n4622)* (defective in serotonin synthesis) and *tdc-1(n3421)* (defective in both tyramine and octopamine syntheses) displayed largely intact CCR during mid-body constraint (Figure S3B), suggesting that serotonin, tyramine, and octopamine are not required for CCR. Mutants *unc-25(e156)* (defective in GABA synthesis) displayed uncoordinated loopy locomotion when moving freely and a compromised CCR (Figure S3B). By contrast, dopamine-deficient *cat-2(e1112)* mutants showed normal locomotion but greatly

impaired CCR (Figure 3C). The deficiency in *cat-2* CCR was fully restored by the addition of exogenous dopamine (Figure 3C), implying that the defect in CCR in *cat-2* mutants is due to the lack of dopamine.

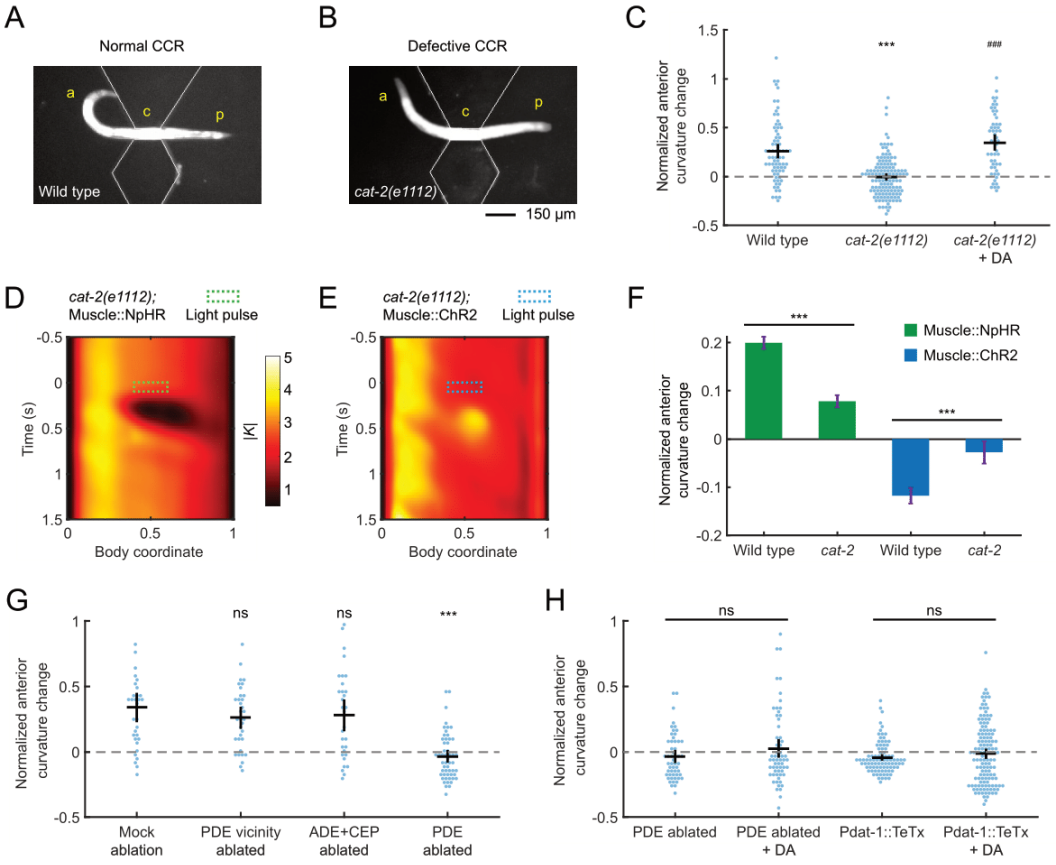

Figure 3. Compensatory curvature response requires functional dopamine signaling by PDE neurons.

(A and B) A wild-type animal (A) and a *cat-2(e1112)* mutant (B) with mid-body confined by a straight-channel microfluidic device, exhibiting undulations with normal and defective CCR, respectively. a: anterior region, p: posterior region, c: constrained middle region of a worm.

(C) CCR indices for wild-type animals and *cat-2(e1112)* mutants in either the absence or presence of exogenous 50 mM dopamine. n ≥ 10 animals per group, mean ± SEM. ***p<0.001 compared with wild type, $^{###}$p<0.001 compared with *cat-2* mutants without exogenous dopamine, Tukey-Kramer multiple comparison tests.

(D and E) Mean absolute curvature around 0.1 s illuminations (dashed box) for *cat-2* mutants expressing Muscle::NpHR (D, n = 133 mid-body illuminations from 33 worms) or Muscle::ChR2 (E, n = 112 dorsal mid-body illuminations from 24 worms).

(F) Normalized anterior curvature change of the first post-illumination curvature peak for wild-type and *cat-2* animals expressing Muscle::NpHR (green) or Muscle::ChR2 (blue), mean ± SEM. ***p<0.001, Student's t-test.

(G) CCR indices for animals with genetic ablation of ADEs and CEPs (*Pdat-1::ICE*, PDE survival confirmed by co-expression of *Pdat-1::RFP*), laser ablation of PDE vicinity regions, and laser ablation of PDEs, compared with a mock-ablation group. n ≥ 10 animals per condition, mean ± SEM. ***p<0.001, ns: not significant, Dunnett's multiple comparison tests.

(H) CCR indices for PDE-ablated worms and transgenic animals expressing tetanus toxin light chain in all dopaminergic neurons (*Pdat-1::TeTx*), in the absence and presence of exogenous 50 mM dopamine, respectively. n ≥ 10 animals per condition, mean ± SEM. ns: not significant, Student's t-test.

In our experiments described above, a worm's mid-body curvature change was induced by optogenetic manipulation or microfluidic constraint. Because the two methods manipulate curvature differently, it is possible that mechanisms for CCR in the two cases are not the same. We asked whether *cat-2* mutants that are defective in CCR in the microfluidic device are also defective in CCR in response to optogenetic perturbation. We crossed the transgenic animals expressing Muscle::NpHR or Muscle::ChR2 into a *cat-2* mutant background and performed the optogenetic muscle perturbation experiments as described above. We found that *cat-2* mutants exhibited impaired CCR to mid-body curvature manipulation by either optogenetic muscle inhibition or stimulation (Figures 3D-F). These results show that dopamine signaling is required for the CCR to both mid-body curvature decrease and increase and support the idea that CCR, as observed in the microfluidic device and optogenetic experiments, reflects the same mechanism.

Dopamine regulates a variety of behaviors in *C. elegans*, including locomotion[76], food detection[71], touch sensation[77], egg laying[58], and gait transitions[72]. The *C. elegans* hermaphrodite has a set of 8 dopaminergic neurons composed of 4 CEPs, 2 ADEs, and 2 PDEs[78]. To test which neuron(s) are required for CCR, we ablated specific subsets of

dopaminergic neurons in L3 larvae and examined their responses to the physical mid-body constraint at their adult stage.

First, we ablated ADEs and CEPs using transgenic animals expressing the human caspase interleukin-1β-converting enzyme (ICE) in the dopaminergic neurons under the *dat-1* promoter[69]. By crossing the *Pdat-1::ICE* strain with a transgene *Pdat-1::mCherry* that expresses RFP in all dopaminergic neurons, and imaging the resulting RFP expression, we verified the cell death of ADEs and CEPs and noted the survival of PDEs (see *Methods*). In addition, we conducted experiments in which we ablated only PDE somas or the vicinity region of PDEs using a focused infrared laser beam[79] (see *Methods*). Transgenic worms with ADEs and CEPs killed or PDE vicinity region damaged exhibited normal CCR, while worms lacking only PDEs were defective in CCR and failed to be restored by exogenous dopamine (Figure 3G and H). These results show that PDEs are the only dopaminergic neurons necessary for CCR.

We further examined transgenic animals with dopaminergic neurons expressing tetanus toxin light chain (*Pdat-1::TeTx*) that blocks synaptic transmission. A compromised CCR was observed in these animals, and adding exogenous dopamine failed to restore this phenotype (Figure 3H). Noting that, in exogenous dopamine environments, CCR was restored in the dopamine synthesis-deficient *cat-2* mutants but not in animals with PDEs eliminated or with TeTx-expressing dopaminergic neurons, our data imply the necessity of functional vesicle release of dopamine from PDE for CCR.

Taken together, these experiments show that dopamine release from PDE, but not from ADE or CEP, is required for CCR.

The dopaminergic PDE neurons respond to mid-body curvature.

The PDE neuron pair is the only dopaminergic neuron type with neurites extending across the mid-body[43], the region where the curvature perturbation was applied. This fact and our finding that PDE neurons are required for CCR led us to speculate that PDEs might function

as proprioceptors for mid-body curvature. A previous study demonstrated that PDE calcium activity in a wild-type animal is phase-locked to its bending waves during roaming[58], but whether PDEs are specifically proprioceptive has not been determined.

As a first step toward establishing a proprioceptive function for PDE, we monitored the spontaneous calcium transients of PDEs in freely crawling animals expressing the genetically encoded calcium indicators GCaMP in PDEs via the *Pdat-1* promoter[58] (Figure 4A; see *Methods*). We observed robust oscillating calcium dynamics in the PDE somas during *C. elegans* forward movement (Figure 4B). We also noticed that the calcium activity in PDE somas was correlated with the animal's body curvature (Figures 4E, orange). These correlations between PDE fluorescence and body posture were not observed in transgenic animals expressing GFP in PDEs (Figure S4). Our calcium imaging experiments indicate that the native neuronal activity of PDEs correlates with body posture during free locomotion of an intact wild-type animal, as previously reported[58].

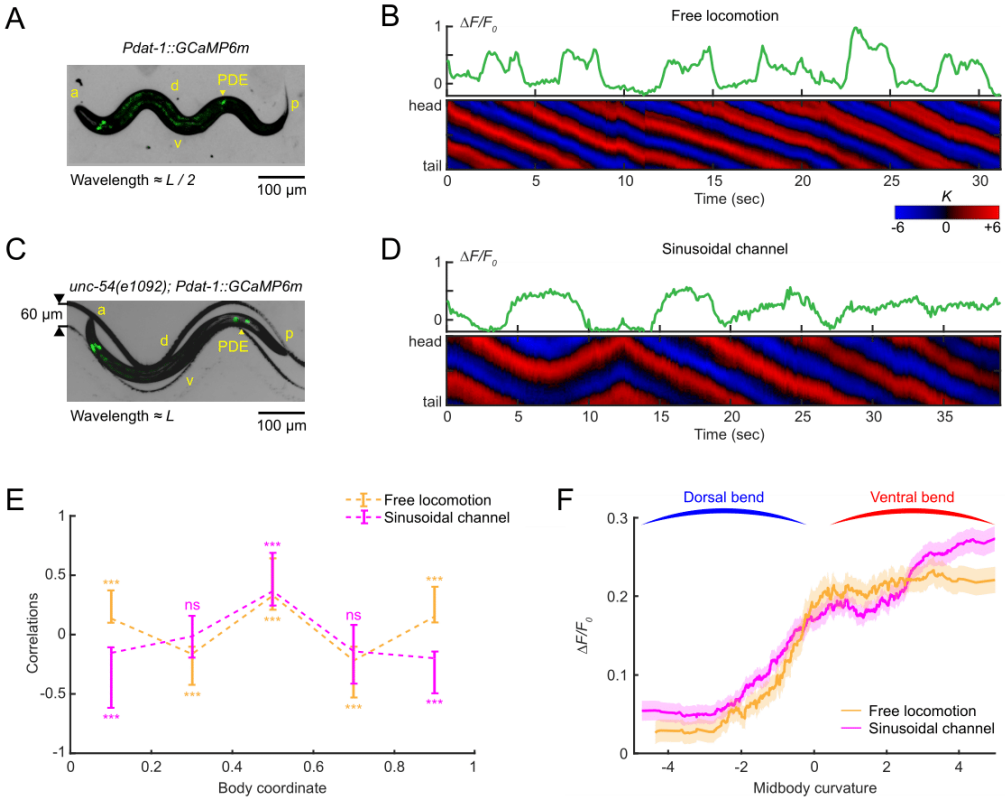

Figure 4. The dopaminergic PDE neurons respond to mid-body curvature.

(A and C) Overlay of a bright field and fluorescence image of the PDE neurons (via transgenic expression *Pdat-1::GcaMP6m*) in (A) a freely moving wild-type animal on an agar surface and (C) a muscularly paralyzed mutant *unc-54(e1092)* within a 60-μm-wide sinusoidal channel. a: anterior, p: posterior, d: dorsal, v: ventral, *L*: worm body length.

(B and D) GCaMP dynamics of PDE (*upper*) and the corresponding curvature dynamics from head to tail (*lower*) for freely moving worms (B) and muscularly paralyzed worms restrained within sinusoidal channels (D).

(E) Cross-correlation between intracellular calcium dynamics of PDE and curvatures of different body regions from head to tail for freely moving worms (orange, n = 12 animals) and channel-restrained worms (purple, n = 20 animals).

(F) Average PDE calcium activity at different values of mid-body curvature for freely moving worms (orange) and channel-restrained worms (purple). Curves were obtained via a moving average along the *x*-axis with 2 in bin width, and the filled area represents a 95% confidence interval.

The finding that PDE calcium activity is correlated with body bending is consistent with but does not itself establish a proprioceptive role for PDE. The activity of other neurons or muscles may influence PDE activity in a manner correlated with but not caused by body bending. To examine whether body bending causes PDE activity, we sought to examine PDE activity in a worm with externally applied bending and deficient muscle contraction. We monitored PDE calcium dynamics in *unc-54(e1092)* myosin heavy chain mutants, which are profoundly defective in muscle contraction. To manually bend the worm body, we constructed a sinusoidal-channel microfluidic device and constrained these worms within the channel (Figure 4C). We then manipulated the worm position through the channel by controlling fluid flow to force the body segments at different curvature values (see *Methods*).

As we moved the paralyzed worm in the channel, we again observed fluctuating PDE calcium dynamics in response to varying induced body posture (Figure 4D). Despite the mutant animals' muscle paralysis, we observed a strong correlation between PDE fluorescence and bending curvature of various body segments (Figure 4E, purple), indicating that body bending is sufficient to induce the neural activity of PDE. We noticed that the curvature-neuronal activity correlation profiles under freely moving and paralyzed conditions

coincided only in the mid-body region (Figure 4E). This observation implies that mid-body might be the spatial receptive field of the proprioceptive response in PDE neurons. Furthermore, by quantifying the dependence of PDE activity on mid-body curvature, we show that PDE calcium levels increased as mid-body curvature varied from a dorsal bend to a ventral bend (Figure 4F), independent of whether the movement was due to muscle contractions of freely moving worms or external forces from sinusoidal channels.

Our experiments demonstrate that PDE neurons proprioceptively sense the mid-body curvature. PDEs have long neurites traveling across the entire body along the ventral side[43]. Since the proprioceptive receptive field of PDE seems to be mid-body, we suggest that PDE neurites near the mid-body region are responsible for the proprioceptive ability of PDE neurons.

Compensatory curvature response requires the D2-like dopamine receptor DOP-3 in AVK neurons.

We next sought to determine what other cellular and molecular components are responsible for CCR downstream of dopamine signaling from PDE neurons.

First, we asked what dopamine receptor(s) are required for CCR. By constraining worms' mid-body in the straight microfluidic channel, we examined CCR behavior in mutant strains, each lacking a single type of dopamine receptor (DOP-1 through DOP-4; Figure 5A) and combinations of the DOP-1, DOP-2, and DOP-3 receptors (Figure 5B). The *dop-3* mutation had a significant negative effect on CCR in all cases tested, and adding exogenous dopamine did not restore CCR in *dop-3* mutants. In contrast, dopamine receptor mutants without the *dop-3* mutation showed normal CCR. Furthermore, we examined the effect of *dop-3* mutation on CCR induced by optogenetic perturbation and found *dop-3* mutants again displayed significant defects in CCR triggered by mid-body muscle inhibition or stimulation (Figures 5C-E). These results show that the D2-like dopamine receptor DOP-3 is required for CCR.

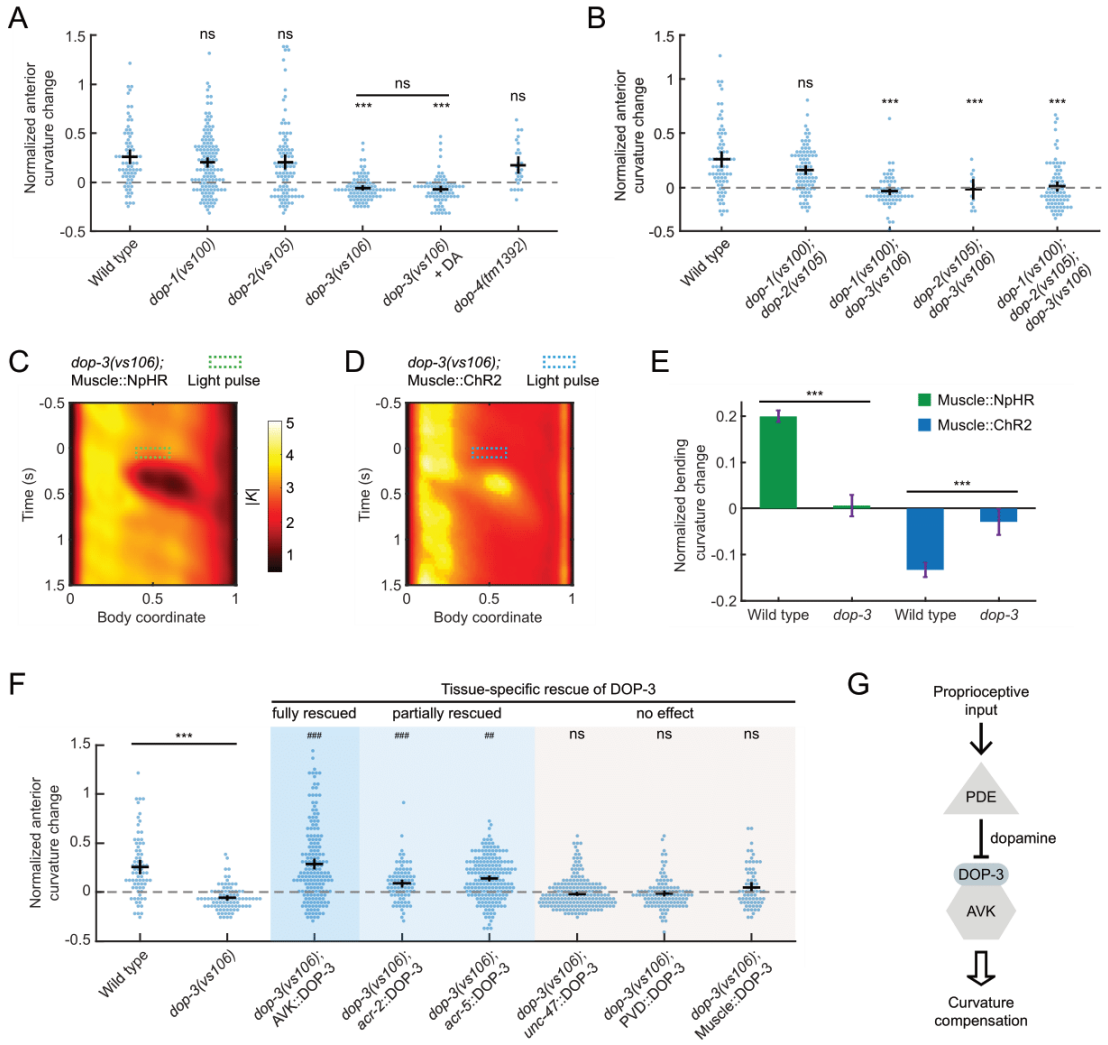

Figure 5. Compensatory curvature response requires the D2-like dopamine receptor DOP-3 in AVK neurons.

(A) CCR indices for wild type and dopamine receptor knockout single mutants *dop-1(vs101)*, *dop-2(vs105)*, *dop-3(vs106)*, and *dop-4(tm1392)* under indicated conditions. n ≥ 10 animals per group, mean ± SEM. ***p<0.001 compared with wild type, Dunnett's multiple comparison tests; ns: not significant when comparing *dop-3* mutants in the absence and presence of exogenous 50 mM dopamine, Student's t-test.

(B) CCR indices for *dop-1 dop-2*, *dop-1 dop-3*, *dop-2 dop-3* double mutants and *dop-1 dop-2 dop-3* triple mutants, compared with wild-type animals. n ≥ 10 animals per indicated condition, mean ± SEM. ***p<0.001, Dunnett's multiple comparison tests.

(C and D) Mean absolute curvature around 0.1 s illuminations (dashed box) for *dop-3* mutants expressing Muscle::NpHR (C, n = 183 mid-body illuminations from 31 worms) or Muscle::ChR2 (D, n = 213 dorsal mid-body illuminations from 33 worms).

(E) Normalized anterior curvature change of the first post-illumination curvature peak for wild-type and *dop-3* animals expressing Muscle::NpHR (green) or Muscle::ChR2 (blue), mean ± SEM. ***p<0.001, Student's t-test.

(F) CCR indices for *dop-3* mutants with DOP-3 function rescued by transgenic expression in AVK neurons (*Pflp-1(trc)::DOP-3*), cholinergic neurons (*Pacr-2::DOP-3*), B-type motor neurons (*Pacr-5::DOP-3*), GABAergic neurons (*Punc-47::DOP-3*), PVD neurons (*Pser-2-prom3::DOP-3*), and body wall muscle cells (*Pmyo-3::DOP-3*), compared with wild type and *dop-3(vs106)* mutants. n ≥ 10 animals per condition, mean ± SEM. ***p<0.001 compared with wild type; ns: not significant, $^{###}$p<0.001, $^{##}$p<0.01 compared with *dop-3* mutants, Tukey-Kramer multiple comparison tests. See *Methods* for rescue criteria.

(G) A model showing mid-body proprioception regulates CCR through DOP-3-dependent dopamine signaling from PDE to AVK neurons.

We asked which cell types expressing DOP-3 are required for CCR. In wild-type animals, DOP-3 receptors are expressed in various cell types, including GABAergic neurons, cholinergic motor neurons, mechanosensory neurons PVD, interneurons AVK, and body wall muscles[62,76]. Using various promoters (see *Key Resources Table*), we expressed DOP-3 in these cell types in a *dop-3* mutant background and tested the ability of the transgenes to rescue CCR (Figure 5F). Restoring DOP-3 expression in GABAergic neurons, PVDs, or body wall muscles failed to rescue the *dop-3* defect (see *Methods* for rescue criteria). We also tested *dma-1(tm5159)* mutants lacking the "menorah" structures in PVD dendrites required for proprioceptive function[64]. We find this mutant maintained a normal CCR (Figure S3B), further suggesting that PVD does not contribute to CCR. However, when we restored DOP-3 expression in AVK neurons[62], the animal's CCR was fully restored to a wild-type level (Figure 5F). A partial rescue in CCR was observed in *dop-3* mutants with DOP-3 expression in cholinergic or B-type motor neurons (Figure 5F). Our rescue experiments suggest that DOP-3 receptors in AVK, and potentially some cholinergic motor neurons,

mediate the proprioception-triggered dopamine signals from upstream PDE neurons to regulate CCR behavior (Figure 5G).

Next, we examined CCR in mutants that disrupt the downstream G protein signaling of DOP-3 and DOP-1 (Figure S3C). Animals with mutations that disrupt the activation of the $G\alpha_o$ pathway (coupled to DOP-3) exhibited defective CCR, whereas mutants with deficiencies in proteins associated with the $G\alpha_q$ pathway (coupled to DOP-1) exhibited normal CCR (Figure S3C; see *Supplemental Information*). DOP-3 and DOP-1 have opposing effects on locomotion by signaling through these two antagonistic G protein pathways, respectively[76]. Given that the DOP-3 receptors, but not the DOP-1 receptors, were found necessary for CCR (Figures 5A,B), our results are consistent with the previously proposed model in which DOP-3 affects locomotion by activating the $G\alpha_o$ signaling pathway[76] (Figure S3D).

These results suggest that CCR requires dopamine signaling through DOP-3 receptors in AVK neurons via $G\alpha_o$ pathways.

The FMRFamide-like neuropeptide FLP-1, released by AVK, regulates SMB motor neurons via receptor NPR-6 to modulate anterior bending amplitude.

We have demonstrated that PDE neurons sense mid-body curvature and that the dopamine/DOP-3 signaling pathway from PDE to AVK is required for CCR. The interneuron AVK mediates FLP-1 FMRFamide-like neuropeptide signaling via the release of dense core vesicles (DCVs) to modulate locomotion in response to various sensory inputs[59,62], and the deletion of the *flp-1* gene results in loopy undulation with an exaggerated sinusoidal waveform in both agar surface[80] and liquid environments (Video S4).

We asked whether AVK and FLP-1 neuropeptide signaling might also be required for CCR. We examined worms with AVK neurons eliminated by laser ablation (see *Methods*) and transgenic animals with AVK expressing tetanus toxin (*Pflp-1::TeTx*) that blocks synaptic vesicle release[62]. Both strains showed superficial wild-type locomotion but strongly

compromised CCR (Figure 6A; Video S5). Next, we tested *flp-1(yn4)* and *flp-1(sy1599)* mutants, both lacking FLP-1 neuropeptide, and *unc-31(e169)* mutants lacking calcium-activated protein for secretion (CAPS, required for neuropeptide release). We found significant defects in CCR in these mutant animals (Figure 6B). These results show that FLP-1 neuropeptide signaling from AVK neurons is required for normal CCR.

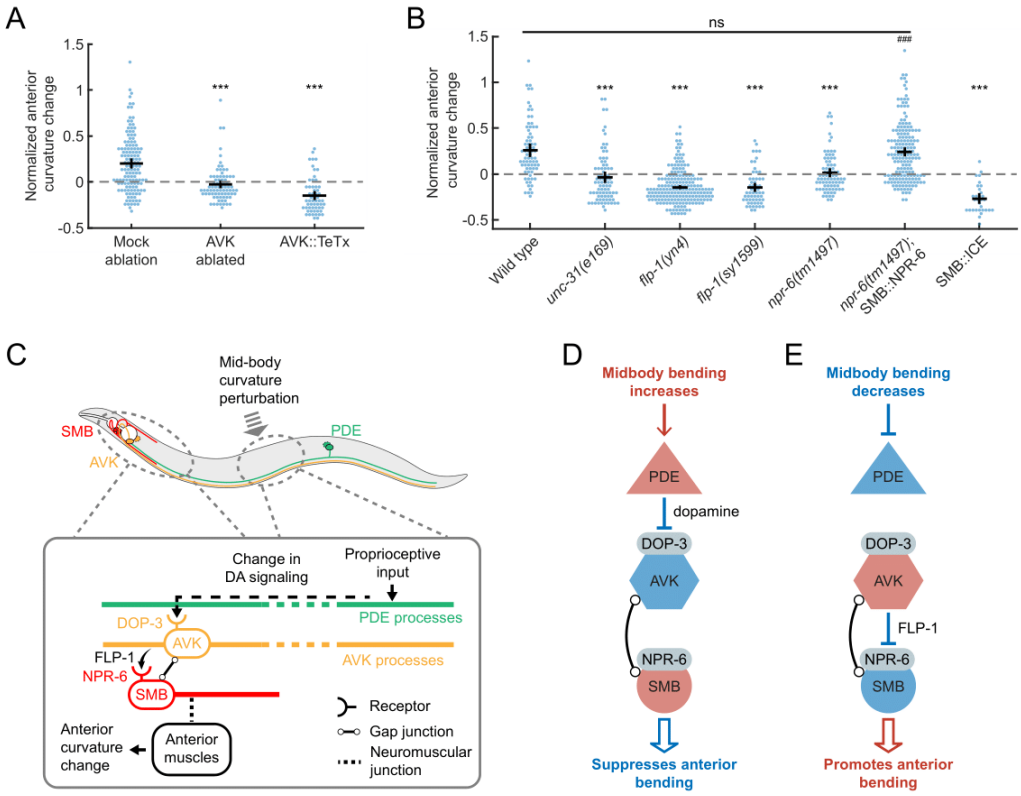

Figure 6. The FMRFamide-like neuropeptide FLP-1, released by AVK, regulates SMB motor neurons via receptor NPR-6 to modulate anterior bending amplitude.

(A) CCR indices for animals with laser ablation of AVK and transgenic animals expressing tetanus toxin in AVK (*Pflp-1::TeTx*), compared with the mock ablation control group. n ≥ 11 animals per condition, mean ± SEM. ***p<0.001, Dunnett's multiple comparison tests.

(B) CCR indices for wild type, mutants *unc-31(e169)*, *flp-1(yn4)*, *flp-1(sy1599)*, *npr-6(tm1497)* and *npr-6* mutants with *npr-6* function rescued by transgenic expression in SMB neurons, and animals lacking SMB (ablation by caspase). n ≥ 12 animals per condition, mean ± SEM. ***p<0.001, ns: not significant, compared with wild type, ###p<0.001 compared with *npr-6* mutants, Tukey-Kramer multiple comparison tests.

(C-E) Models for the mechanisms underlying CCR. (C) (*Upper*) Diagram of PDE (green), AVK (orange), and SMB neurons (red) and their somas/processes within a worm body. (*Lower*) Model for CCR. Dopaminergic neurons PDE transduce the proprioceptive input from the mid-body curvature and signal to AVK neurons via dopamine signaling through DOP-3 receptors. In the anterior region, the AVK neurons signal via FLP-1 neuropeptide to negatively regulate the head-bending-suppressing motor neurons SMB via NPR-6 receptors. Since PDE negatively regulates AVK via dopamine, AVK negatively regulates SMB via FLP-1 peptides, and SMB negatively regulates head bending, perturbation to the mid-body bending leads to a net negative regulatory effect on the anterior bending, as illustrated in two scenarios (D and E). Red and blue indicate excited and inhibited neuronal states, respectively.

The AVK interneurons do not directly innervate muscles to drive body bending. To further probe the circuit underlying CCR, we asked what downstream cells directly affect the anterior bending amplitude while regulated by the upstream FLP-1 signaling from AVK. Previous studies prompted us to speculate that SMB, a class of head motor neurons, might be such a candidate: AVK has both electrical and chemical synapses onto SMB[59], and ablation studies have shown that SMB regulates head and neck muscles and sets the overall amplitude of sinusoidal forward movement[54]. Moreover, SMB activity is regulated by AVK-released FLP-1 signaling through the inhibitory receptor NPR-6[62].

We sought to determine the role of SMB and its peptide-regulated activity in mediating anterior bending amplitude during CCR. We ablated SMB neurons through the expression of a caspase[62], which in previous studies led to a significant increase in body bending amplitude[54] (Video S6). Worms lacking SMBs showed a dramatically impaired CCR (Figure 6B). Next, we examined *npr-6(tm1497)* mutants with and without a transgene that restores the NPR-6 receptor in SMBs[62] and observed restored and defective CCR, respectively (Figure 6B). These experiments support the idea that the SMB motor neurons modulate anterior bending amplitude under the regulation of AVK-released FLP-1 neuropeptide signaling through NPR-6 receptors.

With the previously reported inhibitory effects of dopamine on AVK and FLP-1 on SMB[59,62], our results support the following model for CCR: (1) An increase in mid-body

bending amplitude promotes PDE dopamine release, inhibiting AVK's FLP-1 release via DOP-3 receptor, then causing SMB disinhibition via NPR-6 receptor, leading to a reduction in anterior bending amplitude (Figure 6D). (2) A decreased mid-body bending amplitude suppresses PDE dopamine release, disinhibiting AVK's FLP-1 release, then causing SMB inhibition, leading to an increase in anterior bending amplitude (Figure 6E).

Compensatory curvature response facilitates efficient power expenditure for locomotion.

C. elegans varies its undulatory movements to propel itself through contexts with a wide range of mechanical load[5,81]. We hypothesized that CCR might be responsible for optimal power expenditure during locomotion by modulating undulatory amplitude.

We recorded animals' locomotion in viscous fluids and conducted biomechanical analyses for the strains studied for CCR (see *Methods*). We observed that strains with normal CCR maintained a relatively small curvature amplitude, while strains with defective CCR tended to have larger curvature amplitude (Figure S5A). Based on direct measurements of locomotion, we defined and quantified the power efficiency of undulatory movements as a ratio of the propulsive speed to the total power required during undulations (see *Methods* and *Supplemental Information*). Compared with the wild-type group, strains with either small or large amplitude displayed less efficient power expenditure, characterized by a significant decrease in power efficiency (Figure S5D). By looking at the power efficiency as a function of curvature amplitude in strains with normal CCR, we find the maximal efficiency is achieved at an intermediate curvature amplitude range that is consistent with the peak of the curvature amplitude distribution (Figures S5E, and S6A-D). In CCR deficient strains, however, the peak of the curvature amplitude distribution was not within the optimal amplitude range for power efficiency (Figures S6E-I).

These results suggest that CCR might provide feedback for setting the amplitude of body bending in favor of optimal power usage for forward propulsion. Animals bearing defects in

CCR, however, fail this feedback control mechanism, hence exhibiting higher curvature amplitude and reduced locomotor efficiency.

DISCUSSION

In this study, we described and characterized a proprioception-mediated compensatory mechanism of locomotor control in *C. elegans*. We demonstrate that, during forward locomotion, anterior body bending amplitude compensates for the change in the mid-body bending amplitude by an opposing homeostatic response (Figure 1H). On the circuit level, we analyzed the sensory and modulatory neuronal components and the signaling molecules required for regulating body posture and undulatory dynamics during the compensatory response to perturbations (Figure 6C).

Our calcium imaging results show that dopaminergic neurons PDE proprioceptively sense bending movements of the mid-body, consistent with the observed correlation between PDE activity and undulatory movements of roaming *C. elegans*[58]. Specifically, PDE exhibits a biased body-sensing response, with an elevated calcium level during a ventral bend and a lower calcium level during a dorsal bend (Figure 4F). The specific mechanism that drives these proprioceptive responses in PDE is currently unknown, but the morphological specialization of PDE suggests a proprioceptive function in its long neurites. Determination of this capacity of PDE may be possible through calcium imaging of its subcellular components. Further studies of the effect of genetic mutations of mechanoreceptors expressed in PDE on CCR will also help elucidate the mechanosensitive elements of proprioception, which are likely to be localized in PDE processes near the mid-body.

To clarify the relevant neurotransmitter systems underlying CCR, we examined the role of dopamine neurotransmission by assaying the behavior of dopamine-deficient mutants and their responses to the addition of dopamine. Behavioral tests with exogenous dopamine have been conducted for other studies of *C. elegans* dopamine-related behaviors such as

basal slowing response[71], area-restricted search[69], and gravitaxis[82]. For restoring these behaviors, dopamine might be required at the time just before the behavioral assay or could be required during larval development. These experiments did not clearly distinguish these two roles, as the behaviors of interest in *cat-2* mutants were restored by exposure to exogenous dopamine during behavioral assays and throughout their cultivation. In contrast, CCR in *cat-2* mutants was restored by the presence of exogenous dopamine shortly before the assay (about 3 min), suggesting only an active role for dopamine in the competence of CCR. Failure to rescue CCR by exogenous dopamine for animals lacking or having defective synaptic transmission in PDEs (Figure 3H) further suggests that CCR requires phasic dopamine transmission specifically from PDE.

Our experiments show that the mammalian D2-like receptor DOP-3 is required for CCR. Complete restoration of *dop-3* CCR by genetic DOP-3 expression in AVK neurons indicates that DOP-3 acts in these cells to mediate the effect of dopamine on CCR. In line, eliminating AVK or blocking its synaptic transmission led to a compromised phenotype. We also observed a partial restoration from genetic DOP-3 expression in cholinergic or B-type motor neurons. The reason for these partial rescues is currently unclear, but it may result from a potential AVK expression under these promoters, as indicated by dataset[83]. Alternatively, cholinergic or B-type motor neurons might constitute a parallel circuit acting redundantly to mediate CCR.

Downstream of the PDE dopamine signaling, the CCR circuit comprises the FLP-1 FMRFamide-like neuropeptide signaling from AVK to the head motor neurons SMB that innervate head and neck muscles and regulate the sinusoidal amplitude[54]. Indeed, the underlying circuit (PDE to AVK to SMB) overlaps anatomically and genetically with the circuit for a food-induced behavior[62], where in this case, PDE functions as a mechanoreceptor for the food presence[71] and SMB integrates signals from AVK and DVA that antagonistically affect locomotion in food contexts. Additionally, AVK is involved in several sensory modules that affect locomotion, including food detection[62], oxygen sensation[59,84], chemotaxis[85], and

proprioception (this work). The same neural network controlling behaviors induced from distinct sensations reflects a cellular economy in the *C. elegans* nervous system and high levels of complexity within individual neurons and circuits[86]. An important direction might be to understand how multiple sensory cues get integrated within this PDE-AVK-SMB neuronal module.

In *C. elegans*, proprioceptive information is implicated in generating locomotor rhythms[27]. It is used within the motor circuit to directly propagate the rhythmic bending activity from anterior to posterior segments during forward locomotion[51], indicating that this form of proprioceptive feedback is required to sustain the animal's normal locomotion. However, the proprioceptive information used in CCR is not strictly required for normal locomotion, as most animals with defective CCR still perform superficial wild-type locomotion. We used biomechanical measurements to analyze the effect of CCR on locomotion in viscous fluids. We estimated energy expenditure during forward locomotion and proposed that CCR provides a proprioceptive feedback control mechanism to dynamically maintain bending amplitude within an optimal range for efficient locomotion.

Since animals were tested under off-food conditions, the resulting optimal locomotor efficiency could be important for *C. elegans* exploratory foraging behavior. When *C. elegans* is on food bacteria[87], it performs dwelling behavior with slow forward movements and frequent reversals to remain on the food source[71]. When deprived of food, it will transition to roaming behavior with long forward runs and less frequent reorientations[54,61,69]. CCR could provide a mechanism to minimize the energy an animal expends when in search of food.

Our study reveals that *C. elegans* can modulate and maintain the locomotor amplitude of ongoing locomotion based on its local bending amplitude. Such a form of locomotor homeostasis highlights the behavioral plasticity embedded even within a compact nervous system comprising only 302 neurons[43]. A recent study reported a similar motor control mechanism in adult zebrafish, where a central proprioceptive organ transforms the spinal

cord's local mechanical tension into inhibitory feedback signals that modulate locomotor movements[28]. The neuronal and genetic pathways identified in this behavior may guide further studies investigating neural mechanisms of motor control.

ACKNOWLEDGEMENTS

We are grateful to Niels Ringstad, Kang Shen, Steven Flavell, Andres Villu Maricq, Mei Zhen, Cori Bargmann, Alexander Gottschalk, and Michael Koelle for providing strains and plasmids. Some strains were provided by the *C. elegans* Genetic Center, funded by the NIH Office of Research Infrastructure Programs (P40 OD010440). We thank Gal Haspel, David Raizen, Julia Raizen, Niels Ringstad, Yen-Chih Chen, and Michael Nusbaum for helpful discussions and suggestions. This work was supported by the National Institutes of Health (R01NS084835).

AUTHOR CONTRIBUTIONS

H.J. and C.F.-Y. conceived the project and designed the experiments. H.J. performed most of the experiments and analyses. A.F. established the optical systems for optogenetic experiments and neuron ablation. H.J., Z.L., and A.F. performed the initial experiments regarding the optogenetic muscle inhibition of *C. elegans*. H.J., A.F., and C.F.-Y. provided the code for behavioral analyses. A.R. provided the code for analyzing the calcium activity of moving animals. H.J. and C.F.-Y. prepared the figures and wrote the manuscript. C.F.-Y. conceptualized and supervised the project.

METHODS

KEY RESOURCES TABLE

REAGENT or RESOURCE	SOURCE	IDENTIFIER
Bacterial and Virus Strains		
E. coli OP50	CGC	OP50-1
Chemicals, Peptides, and Recombinant Proteins		
Dextran from *Leuconostoc mesenteroides*	Sigma-Aldrich	D5376
Bovine Serum Albumin	Sigma-Aldrich	N/A
Gibson Assembly Master Mix	NEB	N/A
All-*trans* retinal (ATR)	Sigma-Aldrich	R2500
Poly-dimethyl siloxane (PDMS) + curing agent	Dow Corning	SylGard 184
Experimental Models: Organisms/Strains		
egIs1[Pdat-1::GFP]	CGC	BZ555
cat-2(e1112)	CGC	CB1112
mec-10(e1515)	CGC	CB1515
unc-25(e156)	CGC	CB156
mec-4(e1611)	CGC	CB1611
npr-1(ky13)	CGC	CX4148
eat-16(ad702)	CGC	DA702
npr-6(tm1497)	National Bioresource Project for the Experimental Animal "Nematode *C. elegans*"	F41E7.3
dop-4(tm1392)	CGC	FG58
wzEx664[Pflp-1::TeTx; Pflp-1::mCherry]	Ringstad lab	FQ2747
dma-1(tm5159)	Shen lab	FX5159
flp-11(tm2706)	CGC	HBR507
gpb-2(sa603)	CGC	JT603
goa-1(sa734)	CGC	JT734
dgk-1(sy428)	CGC	JT748
dop-1(vs101)	CGC	LX636
dop-2(vs105)	CGC	LX702
dop-3(vs106)	CGC	LX703
dop-2(vs105); dop-3(vs106)	CGC	LX704
dop-1(vs100); dop-3(vs106)	CGC	LX705
dop-2(vs105); dop-1(vs100)	CGC	LX706
dop-2(vs105); dop-1(vs100); dop-3(vs106)	CGC	LX734
unc-8(e15lb145)	CGC	MP145
tdc-1(n3421)	CGC	MT10549
egl-30(n686)	CGC	MT1434
tph-1(n4622)	CGC	MT14984
egl-10(md176)	CGC	MT8504
del-1(ok150)	CGC	NC279
flp-1(yn-4)	CGC	NY16
ynIs72[Pflp-1::GFP]	CGC	NY2072
flp-1(sy1599)	Ringstad lab	PS8997
egl-8(md1971)	CGC	RM2221
flvEx127[Pdat-1::GCaMP6m; Pmyo-3::mCherry]	Flavell lab	SWF331
trpa-1(ok999)	CGC	TQ233
trp-4(sy695)	CGC	TQ296
mec-4(u253)	CGC	TU253
otIs181[Pdat-1::mCherry; ttx-3::mCherry]; maIs188[Pmir-288::GFP]	Shen lab	TV23560
akEx387[dat-1::GFP; dat-1::ICE]	Villu Maricq lab	VM6365
qhIs1[Pmyo-3::NpHR::eCFP]; qhIs4[Pacr-2::wCherry]	This paper	YX148
cat-2(e1112); qhIs1[Pmyo-3::NpHR::eCFP]	This paper	YX287
dop-3(vs106); qhIs1[Pmyo-3::NpHR::eCFP]	This paper	YX288
cat-2(e1112); hpIs199[Pmyo-3::ChR2::eGFP]	This paper	YX289
dop-3(vs106); hpIs199[Pmyo-3::ChR2::eGFP]	This paper	YX290

dop-3(vs106); qhEx263[Pser-2-prom3::dop-3(+) + Punc-47::GFP]	This paper	YX291
dop-3(vs106); qhEx264[Punc-47::dop-3(+) + Punc-47::GFP]	This paper	YX292
dop-3(vs106); qhEx265[Pacr-2::dop-3(+) + Punc-47::GFP]	This paper	YX293
dop-3(vs106); qhEx266[Pmyo-3::dop-3(+) + Punc-47::GFP]	This paper	YX294
dop-3(vs106); qhEx267[Pacr-5::dop-3(+) + Punc-47::GFP]	This paper	YX295
akEx387[dat-1::GFP; dat-1::ICE]; otIs181[Pdat-1::mCherry; ttx-3::mCherry]	This paper	YX296
kyEx6101[Pdat-1::TeTx::sl2GFP]	Bargmann lab	YX297
unc-54(e1092); flvEx127[Pdat-1::GCaMP6m; Pmyo-3::mCherry]	This paper	YX298
unc-9(fc16); hpEx803[Prgef-1::unc-9cDNA + Podr-1::GFP]	Zhen lab	ZM2509
hpIs199[Pmyo-3::ChR2::eGFP]	Zhen lab	ZM5398
npr-6(tm1497); zxEx850[Pflp-12::LoxP::LacZ::STOP::LoxP::NPR-6::SL2::GFP; Podr-2(18)::Cre]	Gottschalk lab	ZX2037
dop-3(vs106); zxIs20[Pdat-1::ChR2(H134R)::mCherry; Pmyo-2::mCherry]; zxEx1063[Pflp-1(trc)::DOP-3::SL2::GFP; Pmyo-3::CFP]	Gottschalk lab	ZX2201
zxIs29[Pflp-12::Cre; Podr-2(18)::LoxP::ICE; Pmyo-2::mCherry]	Gottschalk lab	ZX3058
Oligonucleotides		
Forward primer for amplifying *dop-3* sequence (GCCAAAGGACCCAAAGGTATGTTTCG)	Ringstad lab	SAZ86
Reverse primer for amplifying *dop-3* sequence (CCGATCTTTCTTGCATCGTGCTCATC)	Ringstad lab	SAZ87
Forward primer for inserting *dop-3* sequence (GTTTGTCAAGAGTTTCGAGGACGG)	Ringstad lab	SAZ88
Reverse primer for inserting *dop-3* sequence (CAAGGGTCCTCCTGAAAATGTTCTAT)	Ringstad lab	SAZ89
Recombinant DNA		
pDC50*(unc-47::dop-3)* [75 ng/µL]	Koelle lab	N/A
pDC66*(unc-47::GFP)* [75 ng/µL]	Koelle lab	N/A
pYX36*(ser-2-prom3::dop-3)* [75 ng/µL]	This paper	N/A
pYX37*(myo-3::dop-3)* [75 ng/µL]	This paper	N/A
pYX38*(acr-2::dop-3)* [75 ng/µL]	This paper	N/A
pYX39*(acr-5::dop-3)* [75 ng/µL]	This paper	N/A
Software and algorithms		
MATLAB	MATLAB Release 2020b	RRID: SCR_001622; https://www.mathworks.com
ImageJ	N/A	RRID: SCR_003070; https://imagej.nih.gov/ij/
Python	Python Software Foundation	RRID: SCR_008394; https://www/python.com

EXPERIMENTAL MATERIALS

C. elegans were cultivated at 20°C on nematode growth media (NGM) plates seeded with *Escherichia coli* strain OP50 using standard methods[88]. For optogenetic experiments, animals were cultivated in darkness on plates with a mixture of OP50 and all-*trans* retinal (ATR). To make OP50-ATR plates, we mixed 2 µm of 100 mM ATR in ethanol into 250 µL suspension of OP50 in LB medium and seeded it onto 6 cm NGM plates. All experiments

were performed with 1-day-old adult hermaphrodites synchronized by hypochlorite bleaching.

Wild-type animals were Bristol strain N2. Transgenic strains for the tissue-specific rescue of *dop-3* function were generated by microinjection of a transgene of DNA clones and a fluorescent co-injection marker (see Key Resources Table).

METHOD DETAILS

Molecular Biology

Plasmid constructs pYX36(*ser-2-prom3::dop-3*), pYX37(*myo-3::dop-3*), pYX38(*acr-2::dop-3*), pYX39(*acr-5::dop-3*) were for tissue-specific expression of DOP-3. The *Pser-2-prom3* (PVD), *Pmyo-3* (body-wall muscles), *Pacr-2* (cholinergic neurons), and *Pacr-5* (B-type motor neurons) promoters were constructed from donor plasmids *Pser-2prom3::GFP* (gift from Kang Shen), *Pmyo-3::RCaMP1h* (gift from Alexander Gottschalk), *Pacr-2::GFP* (gift from Michael Koelle), and *Pacr-5::Arch::GFP* (gift from Shin Takagi), respectively. *dop-3* gene sequence was amplified from pDC50(*unc-47::dop-3*) using primers SAZ86 and SAZ87. Constructs containing promoter sequences were amplified from the corresponding donor plasmids using primers SAZ88 and SAZ89. Reconstruction procedures were conducted using the Gibson Assembly method (Gibson Assembly Master Mix, New England Biolabs). The resulting plasmids were verified by sequencing (ABI 3730XL sequencer, Penn Genomic Analysis Core).

Behavioral Assays

Optogenetic Manipulation Experiments

For experiments with optogenetic manipulation, worms were prepared in a viscous solution using 17% (by mass) dextran in NGM buffer (120 mPa·s viscosity) confined within chambers formed by a microscope slide and a coverslip separated by 125-μm-thick polyester shims (9513K42, McMaster-Carr).

Optogenetic experiments were carried out on a Leica DMI4000B microscope containing a motorized stage. Image sequences were recorded at 50 Hz with an sCMOS camera (optiMOS, Photometrics) under 10X magnification (Leica Plan Fluotar; N.A. 0.30) with dark field illumination provided by red LEDs. We used a custom-built optogenetic targeting system (Fouad et al., 2018) to perform spatially selective optogenetic manipulation of the worm's muscle activity during locomotion. To optogenetically inhibit or stimulate muscles, we used a green (532 nm wavelength) solid-state laser (GL532T3-300, Shanghai Laser & Optics Century) with maximal irradiance of 16 mW/mm^2 or a blue (473 nm wavelength) solid-state laser (BL473T3-150, SLOC) at 10.3 mW/mm^2, respectively.

For optogenetic muscle inhibition and stimulation, we used wild-type and mutant animals with body wall muscles expressing (via *Pmyo-3*) inhibitory opsin *NpHR* and excitatory opsin *ChR2*, respectively. During experiments, each animal was illuminated at indicated regions (illuminating both sides for inhibition, dorsal or ventral side for stimulation) by a brief laser pulse (0.1 s duration, unless otherwise stated) repeated 10 times with a 6 s interval between pulses.

For optogenetic experiments with modulated illuminations, we used pulse durations between 0.1 and 0.5 s, combined with modulated irradiance of laser pulses delivered to animals (3-16 mW/mm^2 for the 532 nm laser, 2.5-10 mW/mm^2 for the 473 nm laser). To modulate the illumination irradiance, we placed two optical polarizers (Vivitar, Thorlabs) in the optical pathway and changed the output light power by rotating the first polarizer.

Microfluidic Experiments

We fabricated two types of custom microfluidic polydimethylsiloxane (PDMS) devices using standard soft lithography techniques[89].

The straight-channel microfluidic device consists of 2000-μm-wide open areas connected by two parallel straight channels (60 μm x 200 μm). The microfluidic chamber was loaded with NGM buffer with 0.1% (by mass) bovine serum albumin (BSA) to prevent worms from

adhering to chamber surfaces or tubing. The sinusoidal-channel microfluidic device consists of a 60-μm-wide sinusoidal channel where the sine wave is 200 μm in height and 400 μm in wavelength. The chamber of this microfluidic device was loaded with an NGM buffer mixed with 0.1% BSA and 17% (by mass) dextran. For both types of microfluidics, we use a 3-way Luer valve (Cole-Parmer) and polyethylene tubing (Saint-Gobain) to connect the chamber of the microfluidic device in parallel to a 1 mL syringe and a reservoir containing NGM buffer. The flow was finely adjusted by turning a screw that slightly compressed the tubing between the chamber and the syringe.

We use straight-channel microfluidics for conducting the CCR assay. Young adults were first transferred to a food-free NGM buffer for about 5 min to wash carried-over bacteria off the animals. Then animals were pipetted from the buffer into the inlet of the microfluidic chamber. To move worms to the field of view (approximately 4 mm x 3 mm), we used the syringe on the inlet to apply pressure or vacuum. Behavior images of each animal in the field of view were recorded for 3 minutes. The worm alternated between constrained and free locomotion, with each mode lasting for about 30 s. Video sequences were recorded at 30 Hz with a 5-megapixel CMOS camera (DMK33GP031, The Imaging Source) and a C-mount lens (Nippon Kogaku NIKKOR-H; effective focal length, 28 mm) using IC Capture software (The Imaging Source). Red LED rings (outer size, 80 mm; Qasim) surrounding the device provided dark field illumination.

We used sinusoidal-channel microfluidics for recording PDE calcium activity in animals with externally-applied bending curvatures. The worm loading and position manipulation were similar to that used in the straight-channel microfluidic device.

Behavioral Data Quantification

General Data Quantification

Processing of the behavioral data from optogenetic and microfluidic experiments was performed using MATLAB custom software (MathWorks) as described in previous

reports[27,73]. The normalized curvature K is the product of κ and the worm body length L derived from the length of the worm centerline. We excluded curvature in the anterior and posterior 5% body regions to avoid high-frequency movements at the ends of a worm. The moving direction of a worm was determined by the gradients in the curvature over time and body coordinate, and image sequences during which the worm moved forward for at least 4 seconds were selected for analysis. The curvature dynamics of the anterior, middle, and posterior regions were defined as the average of the normalized curvature over 0.1-0.3, 0.4-0.6, and 0.7-0.9 body coordinates, respectively.

Quantifying Optogenetic Behavioral Data

To quantify the effect of optogenetic perturbations on worm undulatory amplitude, we calculated the curvature amplitude of the anterior and middle regions, respectively, around each trial of laser illumination. We used the MATLAB function *findpeaks* to identify local extrema along the time-varying curvature profiles. Around each illumination, the corresponding normalized curvature change, defined by $\Delta K_{+n}/|K_{-i}| = (|K_{+n}| - |K_{-i}|)/|K_{-i}|$, was used to quantify the change in curvature amplitude induced by optogenetic perturbations. Here, K_{+n} denotes the value of the n^{th} post-illumination curvature peak. K_{-i} ($i = 1$ or 2) denotes the value of the i^{th} last pre-illumination curvature peak with the same sign as K_{+n}.

Quantifying Microfluidic Behavioral Data

To quantify the effect of straight-channel constraint on worm undulatory amplitude, the whole-body curvature amplitude during constrained locomotion was computed and compared with free locomotion.

We analyzed worm locomotor dynamics of free locomotion to generate an averaged curvature dynamics profile as a function of body coordinates. We evenly divided the worm body coordinate into 10 sections from head to tail (from 0.05 to 0.95, as movements of the anterior and posterior 5% regions were omitted). For each section, we calculated the

average of the normalized curvature over the body coordinate of the section for all periods of free locomotion. Local extrema along each time sequence of curvature were identified (via *findpeaks* function in MATLAB), and the mean of the absolute value of these local extrema was used to denote the curvature amplitude at the body coordinate defined by the mid-point of the section (e.g., 0.1 for section 0.05-0.15). After computing curvature amplitudes for the ten sections, the whole-body averaged curvature amplitude profile, $A_{free}(s)$, was obtained through a linear 1-D interpolation with 100 sample points of values computed across the worm body.

For constrained locomotion, we first used a 3 s time window to divide video sequences of constrained movement into individual short sequences. Due to the unavoidable fluctuations in worm position controlled by the syringe, the constrained body region did not remain fixed. To record the relative position of the constraint with respect to the worm body (gray lines in Figure 3D), we manually marked the channel position in each image sequence.

To calculate normalized curvature change in response to mid-body constraint, we only counted periods during which the anterior and posterior limits of the narrow channel were consistently within 0.35-0.65 body coordinates. We denoted the corresponding curvature dynamics as K_{const}. We took the maximum value of $|K_{const}(s,t)|$ in the time dimension for all qualified short periods and defined the resulting quantity, $A_{const}(s) = |K_{const}(s,t)|$, as the curvature amplitude profile of individual periods. The normalized curvature change of each period is thus represented by $A_{const}(s)/A_{free}(s) - 1$. Additionally, the normalized anterior, mid-body, and posterior curvature changes of individual periods are $\langle A_{const}(s)/A_{free}(s)\rangle|_{0.1}^{0.3} - 1$, $\langle A_{const}(s)/A_{free}(s)\rangle|_{0.4}^{0.6} - 1$, and $\langle A_{const}(s)/A_{free}(s)\rangle|_{0.6}^{0.8} - 1$, respectively ($\langle X(s)\rangle|_a^b$ denotes the average of X in the interval [a b]).

Kinematic and Ethological Analyses of Locomotion

The undulatory wavelength λ and frequency f were calculated by analyzing curvature using methods described in previous studies[5,47].

Using the resistance force theory of slender swimmer[90], we quantified the forward moving speed V_x via the expression[91], $V_x = \alpha_s V_w$, where $V_w = f \cdot \lambda$ is the backward velocity of the undulatory waves relative to the worm body and $\alpha_S = (C_N/C_L - 1)/(2\theta_a^{-2} + C_N/C_L)$ is a nondimensional coefficient depending only on the ratio between the normal and longitudinal drag coefficients C_N/C_L and the peak attacking angle of a body segment with respect to the moving direction θ_a[5]. The ratio of drag coefficients C_N/C_L is set to 1.6 according to previous experimental and theoretical results[63,90].

The muscle power P_m required for undulations is given by[5]:

$$P_m = \frac{1}{2}\left(1 + \frac{1}{sin\phi}\right)(2\pi f)^2 \kappa^2 C_N \left(\frac{\lambda}{2\pi}\right)^4, \#[1]$$

where $\phi = arctan\ arctan\ (2\pi f C_N \lambda^4 / b(2\pi)^4)$ is the phase difference between curvature and the bending torque produced by muscles; C_N is 4587 mPa·s, estimated as 3.3 times the viscosity of the fluid[5].

We defined the power efficiency χ as the ratio of the propulsive speed V_x to the sum of the muscle power P_m and the basal metabolic power P_b, where P_b is set to 60 nW based on the reported values from oxygen consumption rate measurements[92–94].

Laser Ablation of Neurons

Cell ablation experiments (ablation of PDE or AVK neurons) were carried out with a thermal laser ablation system as previously described[79]. Transgenic animals (*Pdat-1::GFP* for PDE ablation; *Pflp-1::GFP* for AVK ablation) at the third larval stage were immobilized on 10% agar pads using 50 nm polystyrene beads and mounted on the microscope[95]. The GFP-labeled somas of target neurons (PDE or AVK) were visualized under GFP fluorescence optics and illuminated with 1~2 laser pulses (1.5 ms duration, 400 mW power) through a 63X oil-immersion objective. After ablation, animals were transferred onto a fresh OP50 plate to recover overnight. The next day, the illuminated animals were again mounted onto the system to confirm the elimination of target neurons. Confirmed animals were transferred

back to seeded plates to resume growth for an additional day until they developed into young adults. For PDE-vicinity ablated group, each worm was lesioned at a proximal region around PDEs (about 5 μm away from the center of the GFP-labeled cell soma) without damaging PDE somas. Mock controls were mounted on the system but not irradiated with the laser.

Calcium Imaging of PDE neurons

For recording PDE calcium activity in freely behaving animals, transgenic worms expressing GCaMP in dopaminergic neurons (*Pdat-1::GCaMP6m*) were picked onto a 5% agar pad with a few microliters of NGM buffer, and covered with a #1.5 cover glass, so that worms were between the agar and the cover glass. Worms moved slowly under these conditions but maintained normal body shape and locomotion. To record PDE calcium activity in paralyzed animals, *unc-54(e1092)* myosin heavy chain mutants expressing GCaMP in PDE neurons (*Pdat-1::GCaMP6m*) were loaded and restrained within a sinusoidal-channel microfluidic device which was filled with 17% dextran solution. The worm position within the channel was manually controlled by a 1 mL syringe connected via polyethylene tubing to induce varying body curvature.

Calcium imaging of PDE in freely behaving and muscularly paralyzed worms was performed on a Leica DMI3000B microscope equipped with a motorized stage (CTR3000, Leica). The GCaMP6m protein in the PDE neurons was excited by the broadband excitation light from a Leica EL6000 illuminator. The worm body was visualized under a dark field illumination provided by the built-in halogen lamp (LH107/2, Leica) through a red filter. To support the simultaneous recording of calcium activity and worm movement, green fluorescence emission and red dark field illumination were collected through a Leica Plan Apo 10X objective (N.A. 0.40), separated by a dual-view beam splitter (DV2, Photometrics) with a GFP/RFP filter set, projected onto an EMCCD sensor (Cascade 1K, Photometrics). The image sequences were streamed at 9 frames per second (fps) acquisition rate under

100 ms exposure time operated by MicroManager software. Approximately 2 min of data were acquired per animal.

Image sequences acquired in either of the worm preparations were processed offline using custom analysis routines. Briefly, each image in these sequences was split in half so that signals obtained through red and green channels were separated into individual sub-images. Each image was background-subtracted and thresholded in the red sub-image sequences to produce a binary image. The binary image sequences were used to quantify worm curvature dynamics using similar methods described above. With the computed curvature dynamics, the corresponding binary image sequences were computationally deformed from a worm shape into a straightened rectangle which provided a mask to crop out whole-body fluorescence signals from the green sub-image sequences. From the masked-out rectangular fluorescent images, regions of interest (ROIs) were selected on somas of the PDE neurons. GCaMP signals were measured as integrated fluorescence over the ROI, subtracted by a background value computed within each recording using a secondary ROI drawn around PDEs but lacking labeled neurons. To obtain normalized signals, the GCaMP values were subtracted and then divided by a baseline F_0 value calculated per recording as the mean of the lowest 50% GCaMP values. Image splitting, binarization, and GCaMP signal extraction were conducted using ImageJ software[96]. Curvature calculation and binary image deformation were performed using custom-written Python scripts.

QUANTIFICATION AND STATISTICAL ANALYSIS

Each transgenic and mutant strain was tested in at least two experiments performed on two days within a week and compared to control experiments done in parallel on the same days. All quantification has been explained within relevant sections of the STAR Methods. Specification of all statistical analyses is reported in the figure legends. Differences were considered to be significant if $p < 0.05$. For DOP-3 rescue experiments, DOP-3 expression of a specific tissue was considered to fully rescue the *dop-3* mutant phenotype if the data

were not significantly different ($p > 0.05$) from the data from *dop-3* mutants assayed in parallel; it was considered as partial rescue if the data were significantly greater ($p < 0.05$) than the data from *dop-3* mutants and significantly smaller ($p < 0.05$) than the data from wild-type animals; it was considered as no effect if the data were not significantly different from the data from wild-type animals.

SUPPLEMENTAL INFORMATION

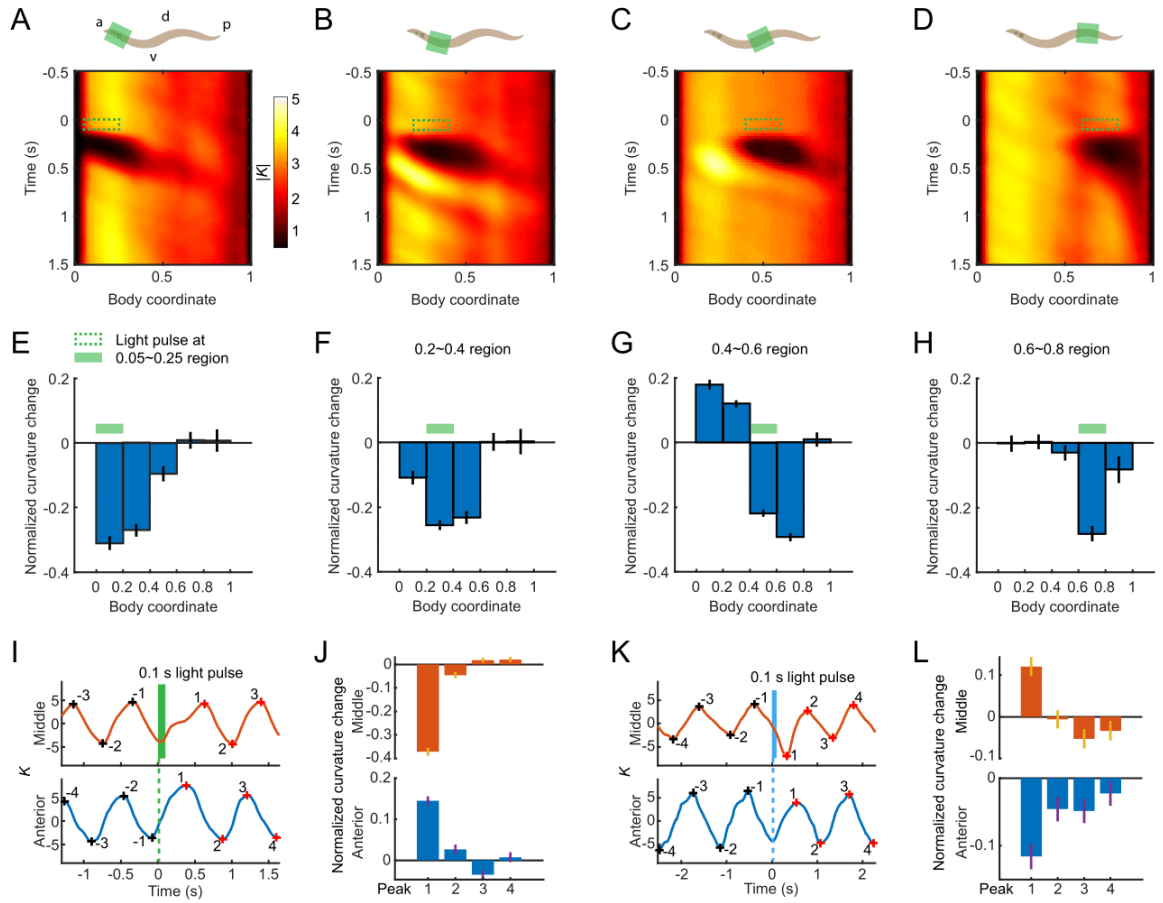

Figure S1. Curvature modulation in response to optogenetic muscle inhibition at various body regions.

(A-D) (*Upper*) Schematics denoting optogenetic muscle inhibition (green bar) applied at head (A), neck (B), middle (C), and posterior (D) regions of transgenic worms expressing Muscle::NpHR. a: anterior, p: posterior, d: dorsal, v: ventral. (*Lower*) Mean absolute curvature. Green box indicates laser illumination. 649 illuminations from 135 worms for (A); 466 illuminations from 75 worms for (B); 1160 illuminations from 206 worms for (C); 467 illuminations from 76 worms for (D).

(E-H) Undulatory amplitude change upon transient optogenetic muscle inhibitions applied at indicated body regions, measured as mean ± SEM of the normalized curvature change of the first post-illumination curvature peak of various body regions from the head to the tail. The green bar indicates a 0.1 s laser illumination applied to the corresponding body region.

(I and K) Curvature dynamics of a worm's middle (*upper*) and anterior (*lower*) regions around a 0.1 s muscle inhibition (I, green) or stimulation (K, blue) in the mid-body. Black and red crosses mark the last 4 pre-illumination and the first 4 post-illumination curvature peaks, respectively.

(J and L) Undulatory amplitude change upon transient mid-body muscle inhibitions (J, n = 1160 mid-body illuminations from 206 worms) or stimulations (L, n = 693 dorsal mid-body illuminations from 122 worms), measured as mean ± SEM of the normalized curvature change of the first 4 post-illumination curvature peaks of the middle (*upper*) and anterior (*lower*) body regions.

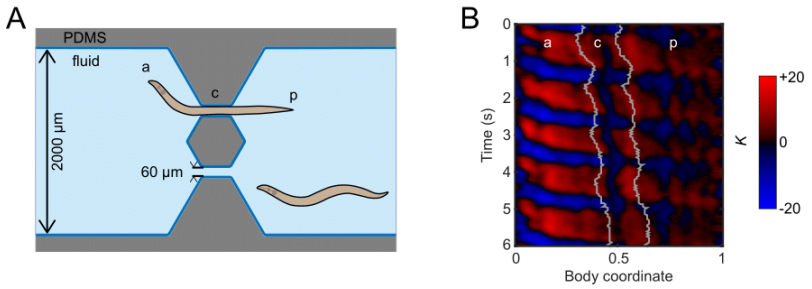

Figure S2. Microfluidics for physically constraining mid-body bending movements during locomotion.

(A) Straight-channel microfluidic device for constraining body curvature. a: anterior region, p: posterior region, c: constrained middle region of a worm.

(B) Curvature of a bout of constrained movements. Gray lines indicate the anterior and posterior limits of the constriction.

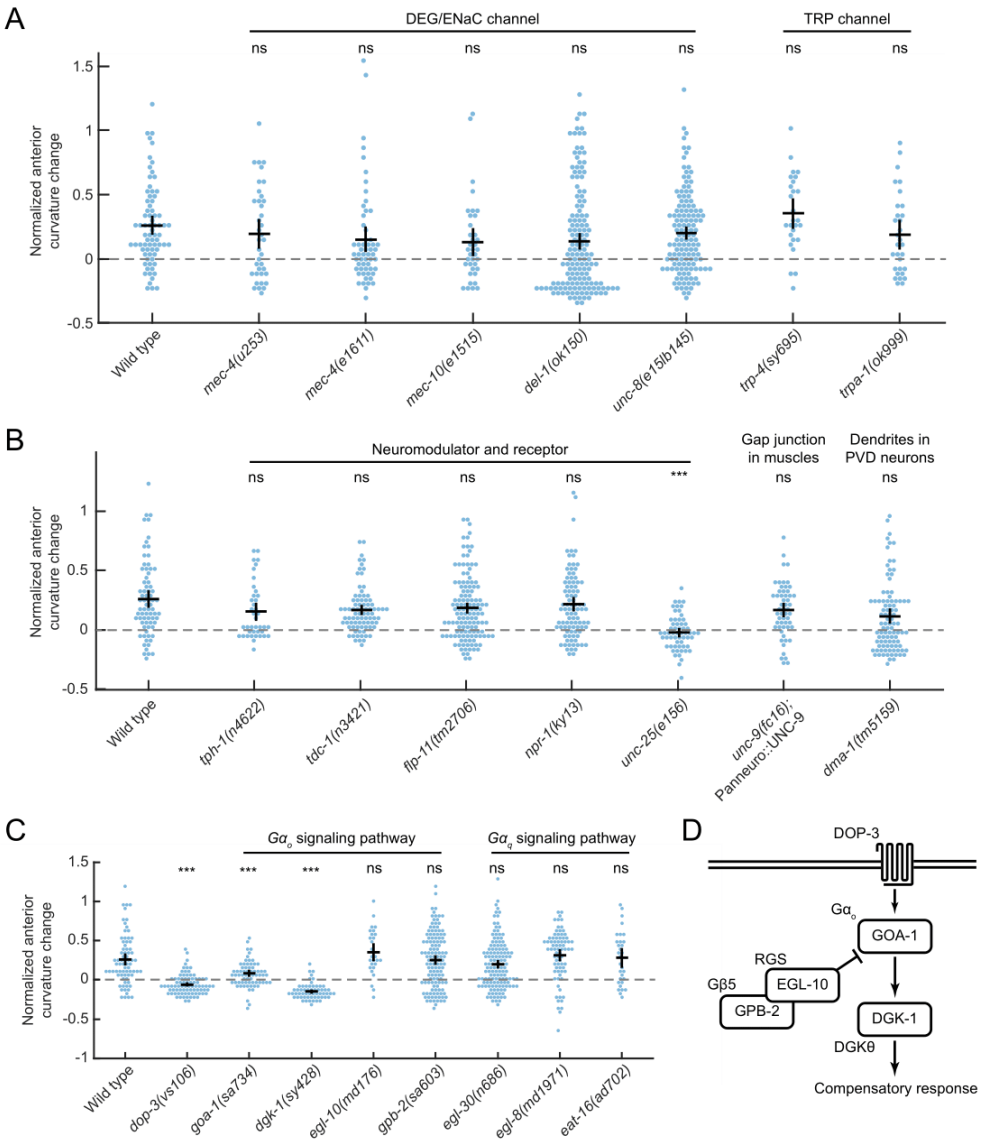

Figure S3. Genetic candidate screening of additional strains for CCR.

(A) CCR indices for DEG/ENaC channel mutants *mec-4(u253)*, *mec-4(e1611)*, *mec-10(e1515)*, *del-1(ok150)*, *unc-8(e15lb145)*, and TRP channel mutants *trp-4(sy695)*, *trpa-1(ok999)*. n ≥ 10 animals per group, mean ± SEM. ns: not significant compared with wild-type animals, Dunnett's multiple comparison tests.

(B) CCR indices for *tph-1(n4622)*, *tdc-1(n3421)*, *npr-1(ky13)*, *unc-25(e156)*, *dma-1(tm5159)* mutants, and *unc-9(fc16)* mutants in which the UNC-9 innexin protein was rescued pan-neuronally. The *unc-9* rescued strain lacks gap junction only in muscle cells. DMA-1 is required to grow the 2°, 3°, and 4° dendrites in the PVD neurons[64]. n ≥ 10 animals per group, mean ± SEM. ***p<0.001, ns: not significant compared with wild-type animals, Dunnett's multiple tests.

(C) CCR indices for *dop-3(vs106)* mutants, $G\alpha_o$ signaling mutants *goa-1(sa734)*, *dgk-1(sy428)*, *egl-10(md176)*, *gpb-2(sa603)*, $G\alpha_q$ signaling mutants *egl-30(n686)*, *egl-8(md1971)*, *eat-16(ad702)*, compared with wild-type animals. n ≥ 10 animals per group, mean ± SEM. ***p<0.001, ns: not significant, Dunnett's multiple comparison tests.

(D) Schematic representation of the $G\alpha_o$ protein signaling pathways that regulate the curvature compensatory response in *C. elegans* (adapted from[76]).

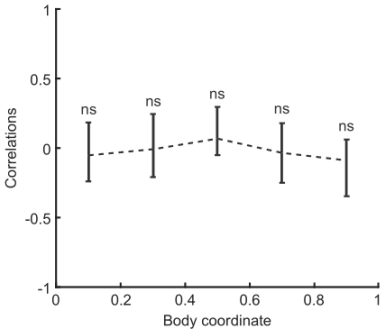

Figure S4. Average correlations of PDE::GFP signal with body curvature of various body regions for freely moving worms. n = 15 animals, mean ± SEM. ns: not significant compared with zero correlation.

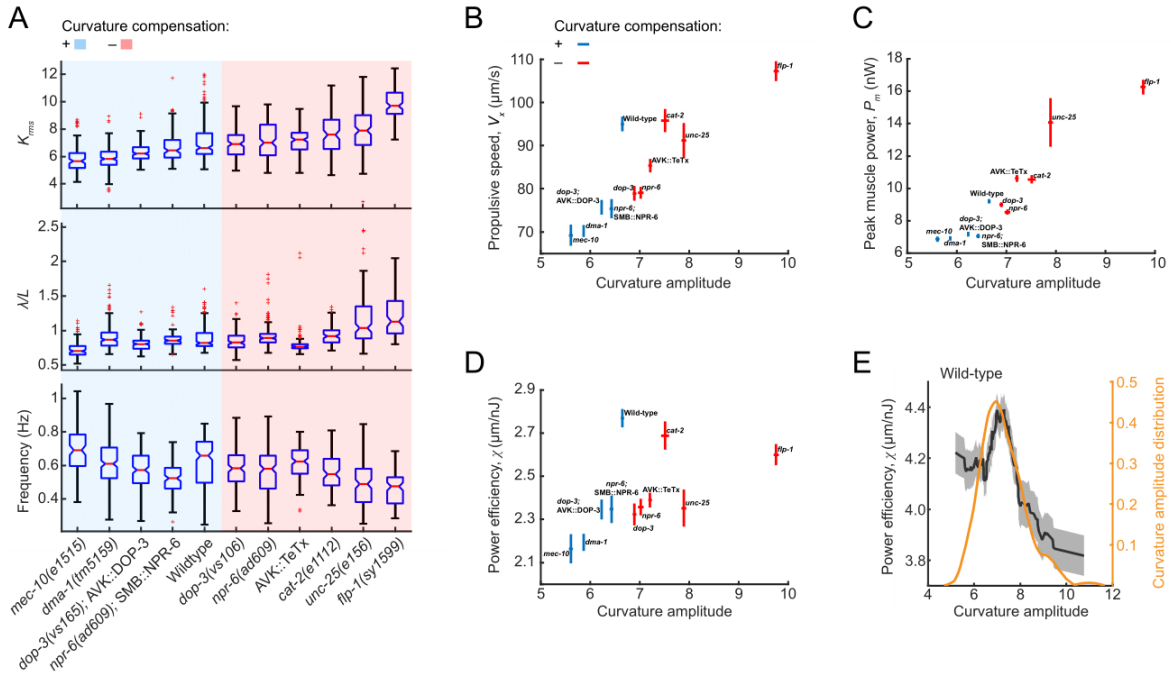

Figure S5. Curvature control for efficient muscle power expenditure.

(A) Locomotory amplitude, wavelength (scaled by worm body length L), and frequency in viscous solutions, measured from selective strains tested for CCR. Cyan and pink panels denote strain groups with normal and defective CCR, respectively. Each box's bottom, mid-line, and top are the data's 25th, 50th, and 75th percentiles. The whiskers go from the end of the interquartile range (between the bottom and top of the box) to the 1.5 times that range away from the bottom or top of the box. Data points beyond the whisker length represent outliers marked as red crosses. n = 100-190 forward moving bouts (10 s duration) from 10-20 animals per group.

(B) Propulsive speed and curvature amplitude (mean $\pm$ SEM), measured from wild-type animals and other strains tested for CCR. Blue and red indicate strains with and without curvature compensation, respectively.

(C) Peak muscle power and curvature amplitude (mean $\pm$ SEM).

(D) Power efficiency and curvature amplitude (mean $\pm$ SEM).

(E) Power efficiency as a function of curvature amplitude (black) and probability density function of curvature amplitude distribution (orange) for wild-type animals (n = 177 forward moving bouts from 30 animals). The χ-K curve was obtained via a moving average along the x-axis with 1.5 in width, and the filled area represents a 95% confidence interval within the bin.

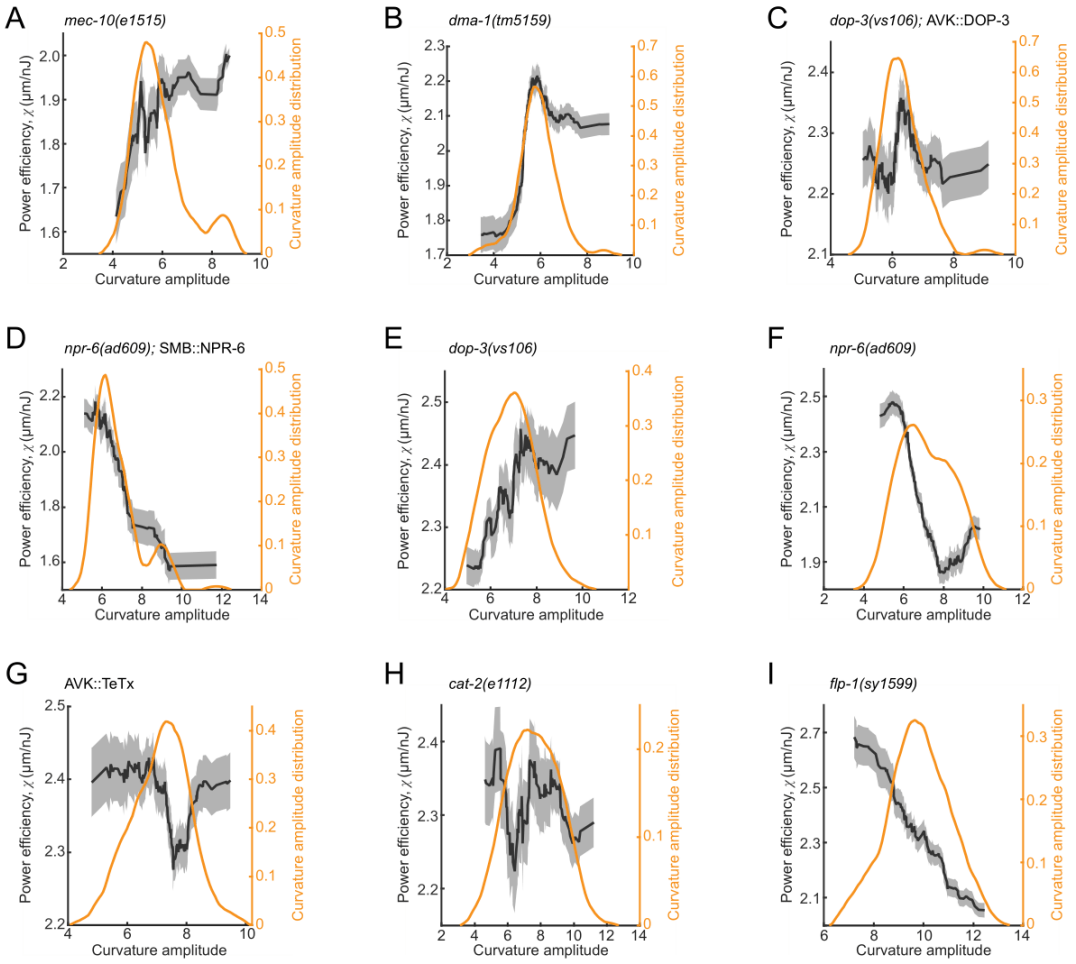

Figure S6. Energetic analyses of additional strains.

Power efficiency as a function of curvature amplitude (black) and probability density function of curvature amplitude distribution (orange) for strains with genotype *mec-10(e1515)* (A, n = 94 forward moving bouts from 16 animals), *dma-1(tm5159)* (B, n = 329 forward moving bouts from 20 animals), *dop-3(vs106);*AVK::DOP-3 (C, n = 200 forward moving bouts from 11 animals), *npr-6(ad609);*SMB::NPR-6 (D, n = 164 forward moving bouts from 10 animals), *dop-3(vs106)* (E, n = 150 forward moving bouts from 14 animals), *npr-6(ad609)* (F, n = 185 forward moving bouts from 11 animals), AVK::TeTx (G, n = 190 forward moving bouts from 12 animals), *cat-2(e1112)* (H, n = 138 forward moving bouts from 14 animals), and *flp-1(sy1599)* (n = 123 forward moving bouts from 9 animals). The χ-K curve was obtained via a moving average along the x-axis with 1.5 in width, and the filled area represents a 95% confidence interval within the bin.

Video S1. Transient optogenetic inhibition of muscles at various regions of the worm body.

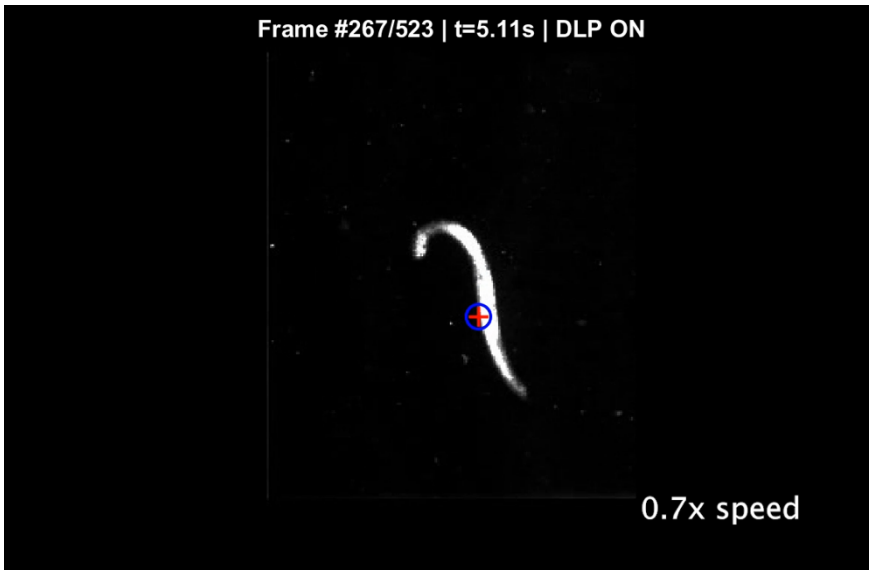

Video S2. Transient optogenetic stimulation of muscle on one side of the middle region of the worm body.

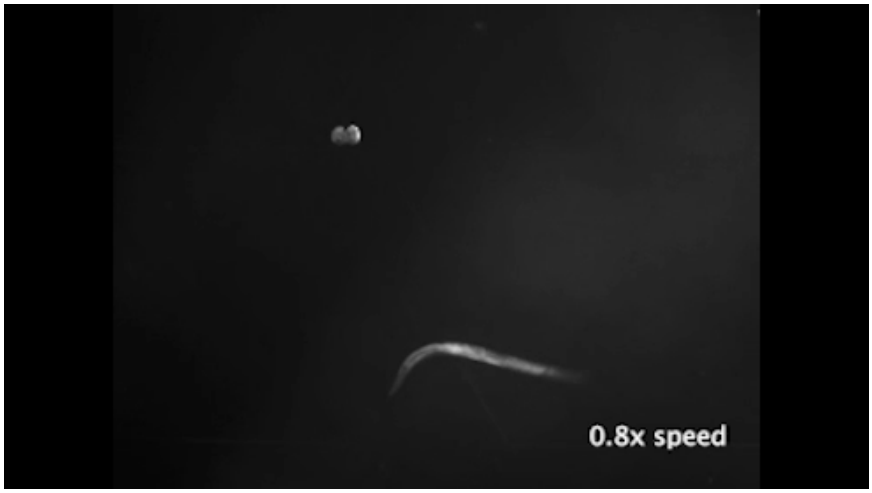

Video S3. CCR of a wild-type animal.

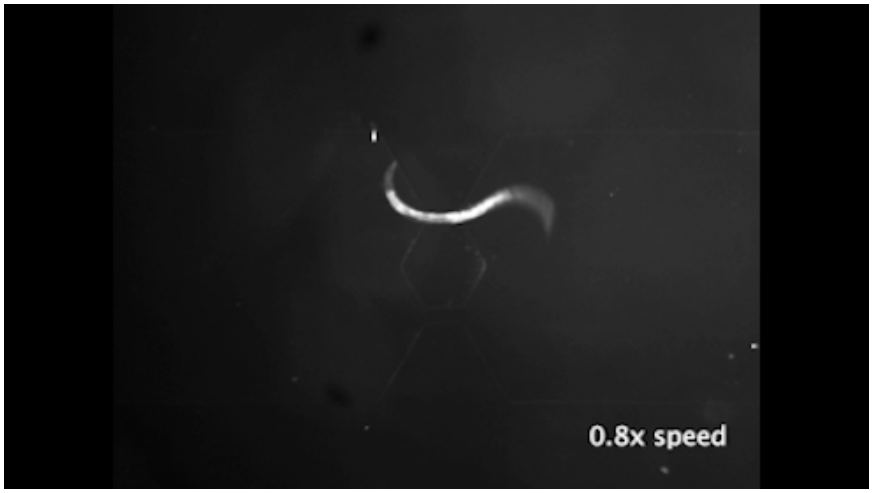

Video S4. CCR of an *flp-1* mutant animal.

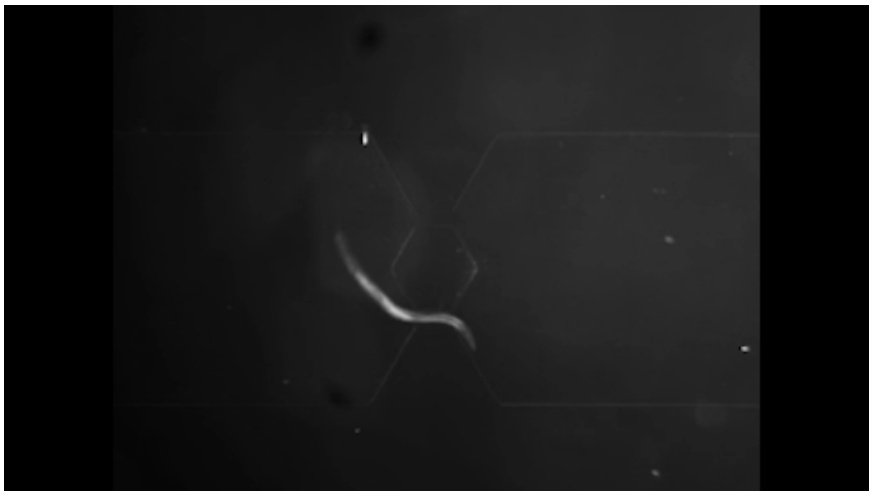

Video S5. CCR of animals with AVK ablated or AVK expressing tetanus toxin.

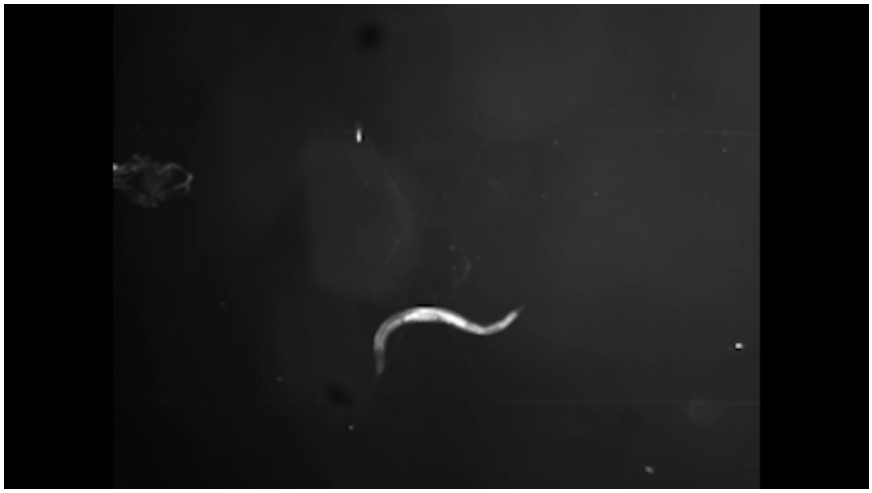

Video S6. CCR of a SMB::ICE transgenic worm.

SUPPLEMENTAL EXPERIMENTAL RESULTS

Kinematic and energetic analyses of undulatory movements

We measured basic kinematic parameters, including undulatory wavelength, frequency, and curvature amplitude of animals immersed in viscous Newtonian fluids (1390 mPa·s). Using the resistance force theory of slender swimmers[90], we used the measured parameters to quantify the forward moving speed in the fluids V_x and the muscle power used for locomotion P_m (see *Methods*).

Among all strains tested, we see that both V_x and P_m positively correlate with curvature amplitude. That is, groups with small (large) mean curvature amplitude displayed low (high) propulsive speed performance supported by low (high) muscle power (Figure S5B,C).

Having characterized the kinematic and energetic parameters of the worm's undulatory movements, we turn to problems that involve the optimization of this mode of locomotion. We hypothesized that the optimal curvature amplitude is the one that maximizes the power efficiency of undulatory movements, which is defined as the ratio between velocity traveled and total power expended (see *Methods*). The total power includes power devoted to locomotion, estimated based on power dissipation, and a basal metabolic rate independent of movement.

CCR analysis of mutants with disruptions in G protein signaling of DOP-3 and DOP-1

We examined CCR in mutants that disrupt the downstream G protein signaling of DOP-3 and DOP-1, the $G\alpha_o$ and $G\alpha_q$ pathways[76] (Figure S3C). Mutants with a deficiency in GOA-1, the *C. elegans* ortholog of the G protein $G\alpha_o$ (coupled to DOP-3), exhibited defective CCR. A similar defect was found in the mutants with a deficiency in the RGS protein DGK-1, a putative downstream effector of GOA-1 $G\alpha_o$.

In contrast, mutants with deficiencies in EGL-10, GTPase activating protein that inhibits GOA-1 $G\alpha_o$, and GPB-2, an obligate subunit of EGL-10 RGS, exhibited CCR to the level of wild type. Mutants with deficiencies in proteins associated with $G\alpha_q$ (coupled to DOP-1) exhibited normal CCR.

REFERENCES

1. Dickinson, M.H., Farley, C.T., Full, R.J., Koehl, M.A.R., Kram, R., and Lehman, S. (2000). How animals move: an integrative view. science *288*, 100–106.

2. Grillner, S., and El Manira, A. (2020). Current principles of motor control, with special reference to vertebrate locomotion. Physiological reviews *100*, 271–320.

3. Pearson, K. (2000). Motor systems. Current opinion in neurobiology *10*, 649–654.

4. Dietz, V., Quintern, J., and Sillem, M. (1987). Stumbling reactions in man: significance of proprioceptive and pre-programmed mechanisms. The Journal of physiology *386*, 149–163.

5. Fang-Yen, C., Wyart, M., Xie, J., Kawai, R., Kodger, T., Chen, S., Wen, Q., and Samuel, A.D. (2010). Biomechanical analysis of gait adaptation in the nematode Caenorhabditis elegans. Proceedings of the National Academy of Sciences *107*, 20323–20328.

6. Forssberg, H. (1979). Stumbling corrective reaction: a phase-dependent compensatory reaction during locomotion. J Neurophysiol *42*, 936–953. 10.1152/jn.1979.42.4.936.

7. Long, J.H., Jr. (1998). Muscles, Elastic Energy, and the Dynamics of Body Stiffness in Swimming Eels1. American Zoologist *38*, 771–792. 10.1093/icb/38.4.771.

8. Mayer, W.P., and Akay, T. (2018). Stumbling corrective reaction elicited by mechanical and electrical stimulation of the saphenous nerve in walking mice. Journal of Experimental Biology *221*, jeb178095. 10.1242/jeb.178095.

9. Tytell, E.D., Carr, J.A., Danos, N., Wagenbach, C., Sullivan, C.M., Kiemel, T., Cowan, N.J., and Ankarali, M.M. (2018). Body stiffness and damping depend sensitively on the timing of muscle activation in lampreys. Integrative and Comparative Biology *58*, 860–873. 10.1093/icb/icy042.

10. Prochazka, A., Sontag, K.-H., and Wand, P. (1978). Motor reactions to perturbations of gait: proprioceptive and somesthetic involvement. Neuroscience Letters *7*, 35–39. 10.1016/0304-3940(78)90109-X.

11. Cohen, A.H., and Wallén, P. (1980). The neuronal correlate of locomotion in fish. Experimental brain research *41*, 11–18.

12. Delcomyn, F. (1980). Neural basis of rhythmic behavior in animals. Science *210*, 492–498.

13. Grillner, S. (2003). The motor infrastructure: from ion channels to neuronal networks. Nature Reviews Neuroscience *4*, 573–586.

14. Kiehn, O. (2011). Development and functional organization of spinal locomotor circuits. Current opinion in neurobiology *21*, 100–109.

15. Kristan, W.B., and Calabrese, R.L. (1976). Rhythmic swimming activity in neurones of the isolated nerve cord of the leech. Journal of Experimental Biology *65*, 643–668.

16. Marder, E., and Calabrese, R.L. (1996). Principles of rhythmic motor pattern generation. Physiological reviews *76*, 687–717.

17. Kiehn, O. (2016). Decoding the organization of spinal circuits that control locomotion. Nature Reviews Neuroscience *17*, 224–238.

18. Rossignol S, Dubuc R, Gossard JP, S. (2006). Dynamic sensorimotor interactions in locomotion. Physiological reviews *86*, 89–154.

19. Windhorst, U. (2007). Muscle proprioceptive feedback and spinal networks. Brain research bulletin *73*, 155–202.

20. Andersson, O., Forssberg, H., Grillner, S., and Wallen, P. (1981). Peripheral feedback mechanisms acting on the central pattern generators for locomotion in fish and cat. Canadian journal of physiology and pharmacology *59*, 713–726.

21. Brodfuehrer, P.D., and Friesen, W.O. (1986). From stimulation to undulation: a neuronal pathway for the control of swimming in the leech. Science *234*, 1002–1004.

22. Friesen, W.O. (2009). Central Pattern Generators: Sensory Feedback. Encyclopedia of Neuroscience.

23. Grillner, S., and Wallen, P. (2002). Cellular bases of a vertebrate locomotor system–steering, intersegmental and segmental co-ordination and sensory control. Brain research reviews *40*, 92–106.

24. Dietz, V. (2002). Proprioception and locomotor disorders. Nature Reviews Neuroscience *3*, 781–790.

25. Boyle, J.H., Berri, S., and Cohen, N. (2012). Gait modulation in C. elegans: an integrated neuromechanical model. Frontiers in computational neuroscience *6*, 10.

26. Iwasaki, T., Chen, J., and Friesen, W.O. (2014). Biological clockwork underlying adaptive rhythmic movements. Proceedings of the National Academy of Sciences *111*, 978–983.

27. Ji, H., Fouad, A.D., Teng, S., Liu, A., Alvarez-Illera, P., Yao, B., Li, Z., and Fang-Yen, C. (2021). Phase response analyses support a relaxation oscillator model of locomotor rhythm generation in Caenorhabditis elegans. eLife *10*, e69905. 10.7554/eLife.69905.

28. Picton, L.D., Bertuzzi, M., Pallucchi, I., Fontanel, P., Dahlberg, E., Björnfors, E.R., Iacoviello, F., Shearing, P.R., and El Manira, A. (2021). A spinal organ of proprioception for integrated motor action feedback. Neuron *109*, 1188–1201.

29. Susoy, V., Hung, W., Witvliet, D., Whitener, J.E., Wu, M., Park, C.F., Graham, B.J., Zhen, M., Venkatachalam, V., and Samuel, A.D. (2021). Natural sensory context drives diverse brain-wide activity during C. elegans mating. Cell *184*, 5122–5137.

30. Grillner, S., Hellgren, J., Menard, A., Saitoh, K., and Wikström, M.A. (2005). Mechanisms for selection of basic motor programs–roles for the striatum and pallidum. Trends in neurosciences *28*, 364–370.

31. Roseberry, T.K., Lee, A.M., Lalive, A.L., Wilbrecht, L., Bonci, A., and Kreitzer, A.C. (2016). Cell-type-specific control of brainstem locomotor circuits by basal ganglia. Cell *164*, 526–537.

32. Svoboda, K., and Li, N. (2018). Neural mechanisms of movement planning: motor cortex and beyond. Current opinion in neurobiology *49*, 33–41.

33. Goulding, M. (2009). Circuits controlling vertebrate locomotion: moving in a new direction. Nat Rev Neurosci *10*, 507–518. 10.1038/nrn2608.

34. Grillner, S., and Jessell, T.M. (2009). Measured motion: searching for simplicity in spinal locomotor networks. Current Opinion in Neurobiology *19*, 572–586. 10.1016/j.conb.2009.10.011.

35. Bourane, S., Grossmann, K.S., Britz, O., Dalet, A., Del Barrio, M.G., Stam, F.J., Garcia-Campmany, L., Koch, S., and Goulding, M. (2015). Identification of a Spinal Circuit for Light Touch and Fine Motor Control. Cell *160*, 503–515. 10.1016/j.cell.2015.01.011.

36. Bui, T.V., Akay, T., Loubani, O., Hnasko, T.S., Jessell, T.M., and Brownstone, R.M. (2013). Circuits for Grasping: Spinal dI3 Interneurons Mediate Cutaneous Control of Motor Behavior. Neuron *78*, 191–204. 10.1016/j.neuron.2013.02.007.

37. Hilde, K.L., Levine, A.J., Hinckley, C.A., Hayashi, M., Montgomery, J.M., Gullo, M., Driscoll, S.P., Grosschedl, R., Kohwi, Y., Kohwi-Shigematsu, T., et al. (2016). Satb2 Is

Required for the Development of a Spinal Exteroceptive Microcircuit that Modulates Limb Position. Neuron *91*, 763–776. 10.1016/j.neuron.2016.07.014.

38. Koch, S.C., Del Barrio, M.G., Dalet, A., Gatto, G., Günther, T., Zhang, J., Seidler, B., Saur, D., Schüle, R., and Goulding, M. (2017). RORβ Spinal Interneurons Gate Sensory Transmission during Locomotion to Secure a Fluid Walking Gait. Neuron *96*, 1419-1431.e5. 10.1016/j.neuron.2017.11.011.

39. Zagoraiou, L., Akay, T., Martin, J.F., Brownstone, R.M., Jessell, T.M., and Miles, G.B. (2009). A Cluster of Cholinergic Premotor Interneurons Modulates Mouse Locomotor Activity. Neuron *64*, 645–662. 10.1016/j.neuron.2009.10.017.

40. Zhang, Y., Narayan, S., Geiman, E., Lanuza, G.M., Velasquez, T., Shanks, B., Akay, T., Dyck, J., Pearson, K., Gosgnach, S., et al. (2008). V3 Spinal Neurons Establish a Robust and Balanced Locomotor Rhythm during Walking. Neuron *60*, 84–96. 10.1016/j.neuron.2008.09.027.

41. Büschges, A., and Mantziaris, C. (2021). Proprioception: Blurring the boundaries of central and peripheral control. Current Biology *31*, R444–R445.

42. Cook, S.J., Jarrell, T.A., Brittin, C.A., Wang, Y., Bloniarz, A.E., Yakovlev, M.A., Nguyen, K.C., Tang, L.T.-H., Bayer, E.A., and Duerr, J.S. (2019). Whole-animal connectomes of both Caenorhabditis elegans sexes. Nature *571*, 63–71.

43. White, J.G., Southgate, E., Thomson, J.N., and Brenner, S. (1986). The structure of the nervous system of the nematode Caenorhabditis elegans. Philos Trans R Soc Lond B Biol Sci *314*, 1–340.

44. Bargmann, C.I. (1998). Neurobiology of the Caenorhabditis elegans genome. Science *282*, 2028–2033.

45. Chronis, N., Zimmer, M., and Bargmann, C.I. (2007). Microfluidics for in vivo imaging of neuronal and behavioral activity in Caenorhabditis elegans. Nature methods *4*, 727–731.

46. Hobert, O. (2003). Behavioral plasticity in C. elegans: paradigms, circuits, genes. Journal of neurobiology *54*, 203–223.

47. Leifer, A.M., Fang-Yen, C., Gershow, M., Alkema, M.J., and Samuel, A.D. (2011). Optogenetic manipulation of neural activity in freely moving Caenorhabditis elegans. Nature methods *8*, 147–152.

48. Croll, N.A. (1970). The behaviour of nematodes: their activity, senses and responses. The behaviour of nematodes: their activity, senses and responses.

49. Von Stetina, S.E., Treinin, M., and Miller, D.M. (2006). The motor circuit. Int. Rev. Neurobiol *69*, 125–167.

50. Zhen, M., and Samuel, A.D. (2015). C. elegans locomotion: small circuits, complex functions. Current opinion in neurobiology *33*, 117–126.

51. Wen, Q., Po, M.D., Hulme, E., Chen, S., Liu, X., Kwok, S.W., Gershow, M., Leifer, A.M., Butler, V., and Fang-Yen, C. (2012). Proprioceptive coupling within motor neurons drives C. elegans forward locomotion. Neuron *76*, 750–761.

52. Kawano, T., Po, M.D., Gao, S., Leung, G., Ryu, W.S., and Zhen, M. (2011). An imbalancing act: gap junctions reduce the backward motor circuit activity to bias C. elegans for forward locomotion. Neuron *72*, 572–586.

53. Chalfie, M., Sulston, J.E., White, J.G., Southgate, E., Thomson, J.N., and Brenner, S. (1985). The neural circuit for touch sensitivity in Caenorhabditis elegans. Journal of Neuroscience *5*, 956–964.

54. Gray, J.M., Hill, J.J., and Bargmann, C.I. (2005). A circuit for navigation in Caenorhabditis elegans. Proceedings of the National Academy of Sciences *102*, 3184–3191.

55. Kaplan, H.S., Thula, O.S., Khoss, N., and Zimmer, M. (2020). Nested neuronal dynamics orchestrate a behavioral hierarchy across timescales. Neuron *105*, 562–576.

56. Schwarz, J., and Bringmann, H. (2017). Analysis of the NK2 homeobox gene ceh-24 reveals sublateral motor neuron control of left-right turning during sleep. eLife *6*, e24846. 10.7554/eLife.24846.

57. Yeon, J., Kim, J., Kim, D.-Y., Kim, H., Kim, J., Du, E.J., Kang, K., Lim, H.-H., Moon, D., and Kim, K. (2018). A sensory-motor neuron type mediates proprioceptive coordination of steering in C. elegans via two TRPC channels. PLoS biology *16*, e2004929.

58. Cermak, N., Stephanie, K.Y., Clark, R., Huang, Y.-C., Baskoylu, S.N., and Flavell, S.W. (2020). Whole-organism behavioral profiling reveals a role for dopamine in state-dependent motor program coupling in C. elegans. Elife *9*, e57093.

59. Hums, I., Riedl, J., Mende, F., Kato, S., Kaplan, H.S., Latham, R., Sonntag, M., Traunmüller, L., and Zimmer, M. (2016). Regulation of two motor patterns enables the gradual adjustment of locomotion strategy in Caenorhabditis elegans. Elife *5*, e14116.

60. Li, W., Feng, Z., Sternberg, P.W., and Xu, X.S. (2006). A C. elegans stretch receptor neuron revealed by a mechanosensitive TRP channel homologue. Nature *440*, 684–687.

61. López-Cruz, A., Sordillo, A., Pokala, N., Liu, Q., McGrath, P.T., and Bargmann, C.I. (2019). Parallel multimodal circuits control an innate foraging behavior. Neuron *102*, 407–419.

62. Oranth, A., Schultheis, C., Tolstenkov, O., Erbguth, K., Nagpal, J., Hain, D., Brauner, M., Wabnig, S., Costa, W.S., and McWhirter, R.D. (2018). Food sensation modulates locomotion

by dopamine and neuropeptide signaling in a distributed neuronal network. Neuron *100*, 1414–1428.

63. Shen, Y., Wen, Q., Liu, H., Zhong, C., Qin, Y., Harris, G., Kawano, T., Wu, M., Xu, T., and Samuel, A.D. (2016). An extrasynaptic GABAergic signal modulates a pattern of forward movement in Caenorhabditis elegans. Elife *5*, e14197.

64. Tao, L., Porto, D., Li, Z., Fechner, S., Lee, S.A., Goodman, M.B., Xu, X.S., Lu, H., and Shen, K. (2019). Parallel Processing of Two Mechanosensory Modalities by a Single Neuron in C. elegans. Developmental cell *51*, 617–631.

65. Bargmann, C.I. (2012). Beyond the connectome: how neuromodulators shape neural circuits. Bioessays *34*, 458–465.

66. Churgin, M.A., McCloskey, R.J., Peters, E., and Fang-Yen, C. (2017). Antagonistic serotonergic and octopaminergic neural circuits mediate food-dependent locomotory behavior in Caenorhabditis elegans. Journal of Neuroscience *37*, 7811–7823.

67. Donnelly, J.L., Clark, C.M., Leifer, A.M., Pirri, J.K., Haburcak, M., Francis, M.M., Samuel, A.D., and Alkema, M.J. (2013). Monoaminergic orchestration of motor programs in a complex C. elegans behavior. PLoS biology *11*, e1001529.

68. Flavell, S.W., Pokala, N., Macosko, E.Z., Albrecht, D.R., Larsch, J., and Bargmann, C.I. (2013). Serotonin and the neuropeptide PDF initiate and extend opposing behavioral states in C. elegans. Cell *154*, 1023–1035.

69. Hills, T., Brockie, P.J., and Maricq, A.V. (2004). Dopamine and glutamate control area-restricted search behavior in Caenorhabditis elegans. Journal of Neuroscience *24*, 1217–1225.

70. Hu, Z., Pym, E.C., Babu, K., Murray, A.B.V., and Kaplan, J.M. (2011). A neuropeptide-mediated stretch response links muscle contraction to changes in neurotransmitter release. Neuron *71*, 92–102.

71. Sawin, E.R., Ranganathan, R., and Horvitz, H.R. (2000). C. elegans locomotory rate is modulated by the environment through a dopaminergic pathway and by experience through a serotonergic pathway. Neuron *26*, 619–631.

72. Vidal-Gadea, A., Topper, S., Young, L., Crisp, A., Kressin, L., Elbel, E., Maples, T., Brauner, M., Erbguth, K., and Axelrod, A. (2011). Caenorhabditis elegans selects distinct crawling and swimming gaits via dopamine and serotonin. Proceedings of the National Academy of Sciences *108*, 17504–17509.

73. Fouad, A.D., Teng, S., Mark, J.R., Liu, A., Alvarez-Illera, P., Ji, H., Du, A., Bhirgoo, P.D., Cornblath, E., and Guan, S.A. (2018). Distributed rhythm generators underlie Caenorhabditis elegans forward locomotion. Elife *7*, e29913.

74. Liu, Q., Chen, B., Gaier, E., Joshi, J., and Wang, Z.-W. (2006). Low conductance gap junctions mediate specific electrical coupling in body-wall muscle cells of Caenorhabditis elegans. Journal of Biological Chemistry *281*, 7881–7889.

75. Schafer, W.R. (2015). Mechanosensory molecules and circuits in C. elegans. Pflugers Arch - Eur J Physiol *467*, 39–48. 10.1007/s00424-014-1574-3.

76. Chase, D.L., Pepper, J.S., and Koelle, M.R. (2004). Mechanism of extrasynaptic dopamine signaling in Caenorhabditis elegans. Nature neuroscience *7*, 1096–1103.

77. Kindt, K.S., Quast, K.B., Giles, A.C., De, S., Hendrey, D., Nicastro, I., Rankin, C.H., and Schafer, W.R. (2007). Dopamine mediates context-dependent modulation of sensory plasticity in C. elegans. Neuron *55*, 662–676.

78. Sulston, J., Dew, M., and Brenner, S. (1975). Dopaminergic neurons in the nematode Caenorhabditis elegans. Journal of Comparative Neurology *163*, 215–226.

79. Fouad, A.D., Liu, A., Du, A., Bhirgoo, P.D., and Fang-Yen, C. (2021). Thermal laser ablation with tunable lesion size reveals multiple origins of seizure-like convulsions in Caenorhabditis elegans. Scientific reports *11*, 1–9.

80. Nelson, L.S., Rosoff, M.L., and Li, C. (1998). Disruption of a neuropeptide gene, flp-1, causes multiple behavioral defects in Caenorhabditis elegans. Science *281*, 1686–1690.

81. Berri, S., Boyle, J.H., Tassieri, M., Hope, I.A., and Cohen, N. (2009). Forward locomotion of the nematode C. elegans is achieved through modulation of a single gait. HFSP journal *3*, 186–193.

82. Chen, W.-L., Ko, H., Chuang, H.-S., Raizen, D.M., and Bau, H.H. (2021). Caenorhabditis elegans exhibits positive gravitaxis. BMC Biology *19*, 186. 10.1186/s12915-021-01119-9.

83. Taylor, S.R., Santpere, G., Weinreb, A., Barrett, A., Reilly, M.B., Xu, C., Varol, E., Oikonomou, P., Glenwinkel, L., McWhirter, R., et al. (2021). Molecular topography of an entire nervous system. Cell *184*, 4329-4347.e23. 10.1016/j.cell.2021.06.023.

84. Zimmer, M., Gray, J.M., Pokala, N., Chang, A.J., Karow, D.S., Marletta, Michael.A., Hudson, M.L., Morton, D.B., Chronis, N., and Bargmann, C.I. (2009). Neurons Detect Increases and Decreases in Oxygen Levels Using Distinct Guanylate Cyclases. Neuron *61*, 865–879. 10.1016/j.neuron.2009.02.013.

85. Suzuki, H., Thiele, T.R., Faumont, S., Ezcurra, M., Lockery, S.R., and Schafer, W.R. (2008). Functional asymmetry in Caenorhabditis elegans taste neurons and its computational role in chemotaxis. Nature *454*, 114–117. 10.1038/nature06927.

86. Chen, B.L., Hall, D.H., and Chklovskii, D.B. (2006). Wiring optimization can relate neuronal structure and function. Proceedings of the National Academy of Sciences *103*, 4723–4728.

87. Brenner, S. (1974). The genetics of Caenorhabditis elegans. Genetics *77*, 71–94.

88. Sulston, J., and Hodgkin, J. (1988). The nematode Caenorhabditis elegans.

89. Xia, Y., and Whitesides, G.M. (1998). Soft lithography. Angewandte Chemie International Edition *37*, 550–575.

90. Gray, J., and Hancock, G.J. (1955). The propulsion of sea-urchin spermatozoa. Journal of Experimental Biology *32*, 802–814.

91. Guo, Z.V., and Mahadevan, L. (2008). Limbless undulatory propulsion on land. Proceedings of the National Academy of Sciences *105*, 3179–3184.

92. Graf, B.L., Kamat, S., Cheong, K.Y., Komarnytsky, S., Driscoll, M., and Di, R. (2017). Phytoecdysteroid-enriched quinoa seed leachate enhances healthspan and mitochondrial metabolism in Caenorhabditis elegans. Journal of Functional Foods *37*, 1–7. 10.1016/j.jff.2017.07.016.

93. Van Voorhies, W.A. (2002). Metabolism and aging in the nematode Caenorhabditis elegans. Free Radical Biology and Medicine *33*, 587–596.

94. Van Voorhies, W.A., and Ward, S. (1999). Genetic and environmental conditions that increase longevity in Caenorhabditis elegans decrease metabolic rate. Proceedings of the National Academy of Sciences *96*, 11399–11403.

95. Kim, E., Sun, L., Gabel, C.V., and Fang-Yen, C. (2013). Long-term imaging of Caenorhabditis elegans using nanoparticle-mediated immobilization. PLoS One *8*, e53419. 10.1371/journal.pone.0053419.

96. Collins, T.J. (2007). ImageJ for microscopy. Biotechniques *43*, S25–S30.